Design and thermal analysis for a novel EMCCD camera payload in a 1U CubeSat form factor

Nicholas B. Angle

Thesis submitted to the Faculty of the
Virginia Polytechnic Institute and State University
in partial fulfillment of the requirements for the degree of

Master of Science
in
Aerospace Engineering

Jonathan T. Black, Chair
Leon K. Harding
Kevin Schroeder

April 26th, 2024
Blacksburg, Virginia

Keywords: CubeSat, EMCCD, thermal, camera, satellite, LEO

Design and thermal analysis for a novel EMCCD camera payload in a 1U CubeSat form factor

Nicholas B. Angle

(ABSTRACT)

Nüvü Camēras, a Canadian company that designs a range of CCD and EMCCD cameras and controllers, recently began development on a miniaturized EMCCD controller for a CubeSat form factor. The detector for this payload requires near-cryogenic temperatures, approximately $188K$, for performance operation. A temperature requirement of that magnitude for a CubeSat form factor is challenging given the low thermal mass, volume, surface area, and power availability for heat storage, dissipation and control systems that would typically be available for larger form factor spacecraft. The goal of this project is to design and perform thermal analysis for the Nüvü Camēras CubeSat EMCCD Controller that allows for cold-biased active temperature control of both the controller electronics and detector. The EMCCD controller had an operational temperature range of $-35°C$ to $+60°C$ while the detector had a performance range of $-110°C$ to $-85°C$ with a desire to maintain a resolution of $\pm 0.25°C$. To meet these requirements, a system was designed within 3D modeling software Autodesk Inventor and imported into Thermal Desktop for thermal analysis and iteration. Models were updated based on thermal analysis results, adjusted by hand, and then tested again until a passive cooling and active heating system that met the requirements was achieved. The final control system was shown to be capable of cooling from $20°C$ ($293.15K$) to $-85°C$ ($188.15K$) and beyond given a Sun Synchronous orbit at $600km$ with attitude control and operational requirements. It was also shown to be capable of heating up, using resistive heaters on key components, beyond the thermal inertia of the system and

environment, indicating viable control on orbit. In the future a PID control method can be implemented, and its use is being investigated by Nüvü Camēras for achieving the desired resolution of $\pm 0.25°C$ in the future.

Design and thermal analysis for a novel EMCCD camera payload in a 1U CubeSat form factor

Nicholas B. Angle

(GENERAL AUDIENCE ABSTRACT)

Nüvü Camēras, a Canadian company that designs a range of Charge-Coupled Device (CCD) and Electron Multiplication Charge-Coupled Device (EMCCD) cameras and controllers, recently began development on a miniaturized EMCCD controller for a CubeSat form factor. CubeSats are a standard for nanosatellites, a classification of spacecraft with dimensions on the order of centimeters instead of meters. The Nüvü Camēras CubeSat EMCCD controller will operate a detector that enables the collection of extremely low light images, or even the counting of individual photons, that other CCD detectors are not capable of in such a form factor. This kind of quality comes with operating requirements such as a very low temperature for the detector, which can be challenging to achieve in a CubeSat. The challenges are the low thermal mass for heat storage, low volume and surface area for fitting components and dissipating heat via radiation, and low power availability to run active systems such as cryocoolers. The goal of this project was to develop a temperature management system that tackles these challenges and allows the operation of the Nüvü Camēras CubeSat EMCCD controller on a variety of Low Earth Orbit (LEO) missions. To achieve this, a passive cooling system was designed to be cooled below the necessary temperature such that it can be effectively warmed back up as a method of active control with resistive heaters. This system was designed in a Computer Aided Design (CAD) program called Autodesk Inventor and analyzed in a thermal analysis program called Thermal Desktop. After a final analysis of

the full setup, it was determined that the system would allow for thermal management at LEO for the Nüvü Camēras CubeSat EMCCD controller and detector.

Dedication

To my wife, co-workers and friends that surrounded me with great advice and the pressure I needed to push through this entire process. Thank you.

Acknowledgments

First and foremost, I would like to thank my co-chair Dr. Leon Harding for his consistent care and attention whenever I needed it despite the chaos in his life while I was writing. Both Dr. Kevin Schroeder and Dr. Harding were invaluable throughout the project and dedicated more time to my work than necessary. I couldn't have asked for better advisors as I worked towards a Master's degree at Virginia Tech. I would also like to thank Dr. Jonathan Black for his time and the opportunity to be here in the first place. Second, I would like to thank the folks at Nüvü Camēras, especially Olivier Daigle and Adam Gilbert, for their patience and time spent dealing with a needy graduate student. I also spent the summer of 2023 writing the majority of this document while working at Kitty Hawk Kites as a hang gliding instructor. It was incredibly challenging maintaining a full-time, very physical job while hitting writing goals each day. My friends, wife, and the hang gliding community at the Outerbanks managed to keep me out of the dark corners of coffee shops and the local library long enough to keep me sane, and for that I owe them a great deal. Finally, thank you to the Aerospace and Ocean Engineering department at Virginia Tech for the opportunity to even write this paper; it has been a huge honor to do the work I have, as well as to work with the amazing people in this wonderful little bubble in Southwest Virginia and Canada.

Contents

List of Figures

List of Tables

List of Abbreviations

ADCS Attitude Determination and Control System

CAD Computer Aided Design

CCD Charge Coupled Device

EMCCD Electron Multiplication Charge Coupled Device

EPS Electrical Power System

FMH Free Molecular Heating

GEVS General Environmental Verification Standard

IR Infrared Radiation

LEO Low Earth Orbit

N/DDD Neutron Irradiation Displacement Damage Dosage

NASA National Aeronautics and Space Agency

NWS National Weather Service

OBC Onboard Computer

PID Proportional-Integral-Derivative

SEE Single Event Effect(s)

SSO Sun Synchronous Orbit

SSRI Small Satellite Reliability Initiative

TID Total Ionizing Dose

TRL Technology Readiness Level

TVAC Thermal Vacuum

CCD is a class of sensor used in imagers such as commercial digital cameras. Typically seen as a metal oxide semiconductor chip that transports electrons generated via the Photoelectric effect to a register that generates an image digitally.

EMCCDs, or Electron multiplication CCDs, are a version of the typical CCD with an added register in the process that stimulates the addition of extra electrons with a high voltage charge booster. This allows a discrete signal of 20 photo-electrons to turn into a readable signal of thousands of electrons, and thus effective low-light imaging.

PID is a control method that involves taking an input signal and running it through three modification stages: Proportional, Integral, and Derivative. These stages modify the error signal, or the output signal subtracted from the user defined input signal, in three ways. The following equation defines the PID control variable, $u(t)$: $u(t) = K_p e(t) + K_i \int e(t)dt + K_d \frac{de(t)}{dt}$, where K_p, K_i, and K_d are the user defined weight coefficients for the proportional, integral, and derivative terms, respectively.

The National Weather Service (NWS) is the leading US-based prediction and modeling center for the weather. It regularly uses satellite data for use in atmospheric modeling, and is a great source for data on the Earth's atmosphere in general.

NASA, or the National Aeronautics and Space Agency, is the United States federal entity that handles research and development for aircraft, spacecraft, astronomy, and space science.

LEO, or Low Earth Orbit, is a broad region around the Earth defined by an altitude band. LEO is defined by NASA as any orbit with an altitude below 1,200 miles, or 2,000 kilometers. For highly eccentric orbits this includes any apoapsis that has an altitude less than 2,000 kilometers.

SSO, or Sun Synchronous Orbit, is a special orbit that lies with the LEO altitude band but has an inclination requirement of 97.94° at an altitude of 600 kilometers. This makes it a polar orbit, in that it crosses over the poles of the Earth, as well as a retrograde orbit. A retrograde orbit is one that has a component of its revolution in the opposite direction to that of the Earth's rotation. This orbit is unique, and useful, in that a satellite will pass over some point on the surface at the same local time each revolution, in mean solar time. This provides similar illumination characteristics for an imager on a given point on the surface of the Earth.

FMH, or Free Molecular Heating, is a subset of convective heating in the very low-density regime of a gaseous medium, i.e. where the mean free path of the molecules in the medium are large compared to the distances between collision surfaces. High energy particles in a medium, such as the Earth's atmosphere, impact the surface of a spacecraft and transfer energy. Collisions between particles in the medium are few while traversing between surfaces.

TRL, or Technology Readiness Level, is a measurement of the heritage of a concept or technology. This ranges from TRL-1, basic concept or idea, to TRL-9, the operation of technology on-site or on-orbit. This is defined by NASA's JPL (Jet Propulsion Laboratory), and serves as a means to track the development of technology intended for use in spacecraft, and for the spacecraft itself.

CAD, or Computer Aided Design, is the use of the processing and graphical power of a computer to draft engineering technology previously done by hand. CAD programs includes

2D and 3D modeling software such as Autodesk AutoCAD and Inventor, Solidworks, or Ansys SpaceClaim.

SSRI, or the Small Satellite Reliability Initiative, is a public-private community driven project to catalogue information and technology development progress for CubeSats to reduce small satellite mission risk.

IR, or Infrared Radiation, is photon radiation with a wavelength of 1000μm to 0.7μm. The term infra-red stems from the wavelength band being below the red region of the visible spectrum. IR can also stand for just Infra-Red, omitting the radiation term, for simplicity.

The EPS, or Electrical Power System, is the power management and distribution system (PMAD) of a spacecraft. The system in general can be referred to as the PMAD system, but many CubeSat component manufacturers refer to this as the EPS.

The OBC, or Onboard Computer System, is the operational processing electronics for a spacecraft. This terminology is commonly seen in CubeSat components, but covers a broad band of components for spacecraft in general.

The ADCS, or Attitude Determination and Control System, is the set of components that allow for attitude maneuvers in a spacecraft. These often consist of gyroscopic control systems and thrusters, along with sensors for attitude detection.

TVAC, or Thermal Vacuum, is most often used as TVAC Chamber and refers temperature and vacuum testing done on components to see how they operate at different temperatures and in different pressures simultaneously.

GEVS, or General Environmental Verification Standard, is the NASA-defined testing standard for air- and spacecraft components. The standard includes vibration, vacuum, temperature, and other operational testing requirements.

TID, or Total Ionizing Dose, is the summation of the overall accumulated dose from various sources including electrons, protons, heavy ions, x-rays, gamma rays, and more.

N/DDD, or Neutron Irradiation Displacement Damage Dosage, is the accumulated dose from non-ionizing neutron displacement events. Neutrons can not induce TID damage directly, but can do so indirectly through secondary events from spallation reactions.

SEE, or Single Event Effects, are caused by a single energetic particle and can take on many forms. Single Event Upsets (SEUs) are soft errors and non-destructive, often taking the form of transient pulses in logic or as bit flips in memory. Single Event Latch-ups (SELs) are hard errors and potentially destructive: they can result in a high operating current potentially above operation requirements/thresholds and must be cleared by a power reset. Other effects include Single Event Burnouts (SEBs) of MOSFETs, frozen bits, and noise in CCDs.

Chapter 1

Review of Literature

1.1 Study Background/Context

1.1.1 LEO Radiation Environment

A key but often overlooked aspect of spacecraft engineering within general public knowledge is thermal management. Every component of a spacecraft will be sensitive to its temperature to some degree, driven primarily by the electronics needs such as maximum and minimum junction temperature or battery cell temperature. Components that sit beyond their temperature limits can cease functioning and even experience irreversible damage. Management of the temperature of spacecraft is done through load balancing, much as the Earth itself has a thermal balance, i.e. the energy put into the system matches the energy put out by the system. Thermal power, measured in Watts or Joules per second, is the standard metric for designing a control system and represents the scalar rate at which thermal energy is moved through the system [32]. Using the Earth as an example, there are thermal loads, or contributors, both internal and external, that must be accounted for. The NWS [26] provides a helpful image for visualizing the thermal balance between the Earth, its atmosphere, and space below in Figure 1.1.

The energy emitted by the Sun enters the Earth's atmosphere, where it is both reflected and absorbed to some degree by the clouds. Some of the energy makes it through the atmosphere

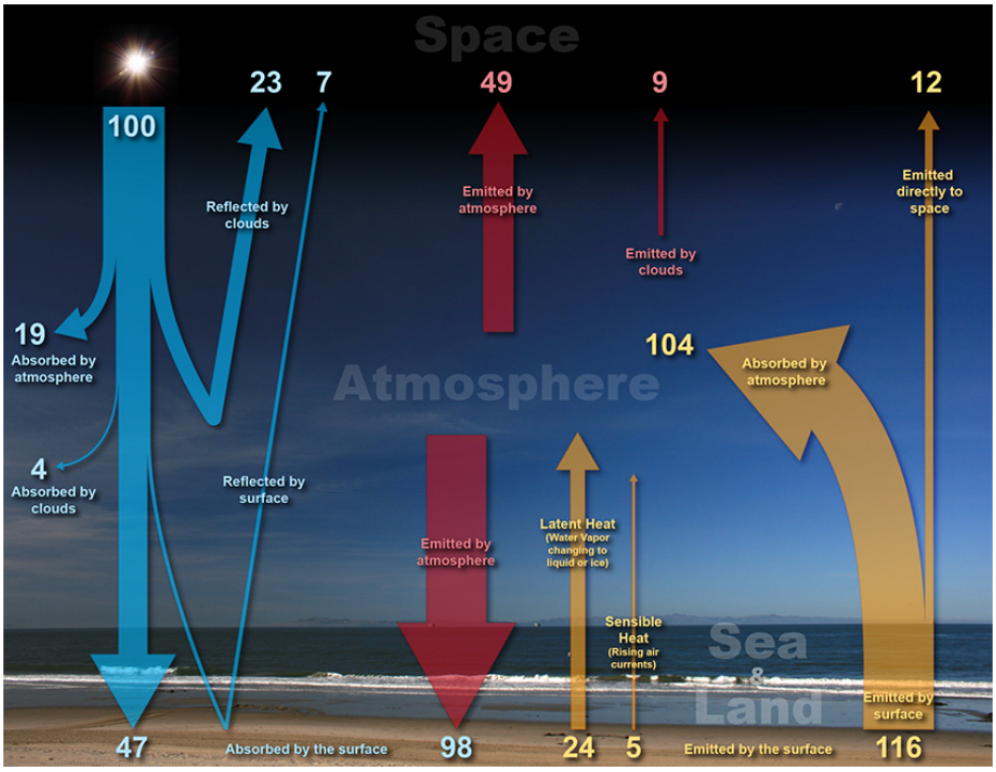

Figure 1.1: National Weather Service Earth-Atmosphere-Space Thermal Balance [26]

and interacts with the Earth's surface, where it is also both absorbed and reflected to varying degrees based on local conditions such as surface albedo, defined here as the reflectivity of the surface, and topography [19]. Both the atmosphere and the surface of the Earth emit energy in the form of long wavelength photons, most typically in the infrared spectrum, based on their temperature as gray body emitters, which will be covered in depth later. This energy is likewise absorbed or reflected by the Earth's surface and atmosphere, and is considered an internal source of thermal energy. Some of this energy emitted by the Earth's surface is caught in the atmosphere in the form of warm, rising air or seen as latent heat from the transition of water vapor into liquid or solid form. Most of this energy will be in the form of infrared light that is repeatedly emitted at the surface, absorbed by the clouds and reflected or re-emitted back to the surface and so on until it finally travels back into space. All of this energy can be accounted for, and the NWS [26] provides an approximation

of the contributions at each stage in Tables 1.1 - 1.3 below.

Table 1.1: Space-atmosphere interface, incoming solar energy vs. outgoing energy [26]

Incoming Energy (%)		Outgoing Energy (%)	
Value	Source	Value	Source
+100	Shortwave Radiation from the Sun	-23	Shortwave reflected back to space by atmosphere
		-7	Shortwave reflected back to space by surface
		-49	Longwave radiation into space by the atmosphere
		-9	Longwave radiation from clouds into space
		-12	Longwave radiation from surface into space
+100	Total Incoming	-100	Total Outgoing

Table 1.2: Within the atmosphere, incoming energy vs. outgoing energy [26]

Incoming Energy (%)		Outgoing Energy (%)	
Value	Source	Value	Source
+19	Shortwave radiation in the atmosphere	-9	Longwave radiation to space from clouds
+4	Shortwave radiation by clouds	-49	Longwave radiation to space from atmosphere
+104	Longwave radiation from the surface	-98	Longwave radiation to surface from atmosphere
+5	Convective Currents and local churning in atmosphere		
+24	Condensation/Deposition of water vapor in the atmosphere		
+156	Total Incoming	-156	Total Outgoing

Table 1.3: Atmosphere-surface interface, incoming energy vs. outgoing energy [26]

Incoming Energy (%)		Outgoing Energy (%)	
Value	Source	Value	Source
+47	Shortwave Radiation from the Sun	-116	Longwave radiation emitted by the surface
+98	Longwave radiation from atmosphere	-5	Removal of heat via convection
		-24	Heat for phase change of water on surface
+145	Total Incoming	-145	Total Outgoing

The energy balance of a spacecraft is similar to that of the Earth, but it will have no atmosphere and thus simplify to three subsystems: the spacecraft internal components, the surface of the spacecraft, and space. Spacecraft can inhabit any region of space, from a very low orbit of the Earth all the way to interstellar space. However, for the purposes of this paper the focus is on the Low Earth Orbit (LEO) environment and the corresponding heat sources that a spacecraft can experience there. The primary heat sources on orbit for a spacecraft are direct solar radiation, albedo radiation, and planetary infrared radiation. However, two more sources exist that have a smaller but just as important impact: free molecular heating and charged particle heating. Free molecular heating occurs when a spacecraft is encountering the fringes of the Earth's atmosphere, both the neutral atmosphere and the charged ionosphere. Within both the neutral atmosphere and the ionosphere the spacecraft can interact with atmospheric particles as though it were an inelastic collision due to the near-vacuum density of the LEO environment and experience heat transfer [29]. A free molecular process unique to the ionosphere is the recombination of high-energy particles at or near the surface of the spacecraft, which also contributes to the free molecular heating effect [14]. Charged particle heating is a volumetric heating effect caused by high-energy particles passing through the surfaces of the spacecraft and interacting directly with the volume of

the spacecraft via collisions, thus transferring heat [17]. This makes it important to consider the expected radiation environment of the spacecraft orbit for the intended lifetime of the mission, especially if near-cryogenic and cryogenic components are in use. It is also important to remember that open, or deep, space is considered a heat sink and that when exposed to nothing but deep space a surface will have a large negative heat load, or experience heat loss. The equivalent temperature of deep space is defined as the gray body temperature of the cosmic microwave background, which is approximately 2.73 Kelvin, or -270.42°C [11]. Spacecraft can also achieve net negative in terms of heating when they pass into the shadow of a large body, or eclipse, such as that of the Earth. At that point heat sources such as direct solar and albedo radiation disappear, leaving only much less significant factors such as planetary infrared radiation, free molecular heating and charged particle heating.

1.1.2 Heat Transfer

Conduction

Thermal energy can be transferred via three mechanisms: conduction, convection, and radiation. Conduction is the transfer of thermal energy, or the rate of change of the average kinetic energy for a given volume of particles, by direct interaction within a solid medium [3]. This solid medium will have some natural conductivity value, k, dependent upon its material, that describes how efficiently it allows for heat transfer within itself. Thermal conductivity is the reciprocal of thermal resistivity, $r = \frac{1}{\kappa}$, which is analogous to electrical conductivity and resistivity.

For an example of steady state conduction, take a finite rectangular wall section with an area, A, and hold both sides to differing but constant temperatures, as seen below in Figure 1.2 [10]:

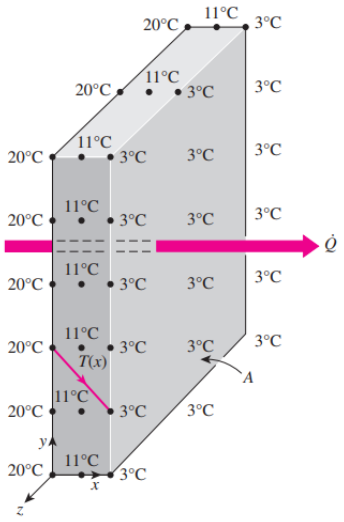

Figure 1.2: Steady State Finite Wall Conduction Setup [10]

In this system, the temperature only differs in the x-axis, making the heat transfer one dimensional. The amount of thermal energy going into the system must be the same as the energy leaving the system to maintain these temperatures, or:

$$\frac{dQ}{dt}_{in} - \frac{dQ}{dt}_{out} = \frac{dE_{Wall}}{dt} = 0, \tag{1.1}$$

Where,

$$Q = \text{Thermal Energy, in Joules [J]}$$

$$E_{Wall} = \text{Energy of the wall, in Joules [J]}$$

Thus,

$$\frac{dQ}{dt}_{cond} = \text{Constant, for a steady state system.} \tag{1.2}$$

To provide a specific example, take a wall section with thickness L, area A, and average thermal conductivity k. The two surfaces of the wall are maintained at temperatures T_1 and T_2, so for one-dimensional heat transfer there is $T(x)$, as shown below in Figure 1.3 [10].

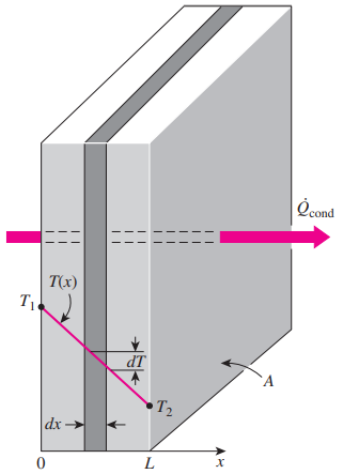

Figure 1.3: Example of One-Dimensional Heat Transfer through Rectangular Wall Section [10]

Then, Fourier's Law of Heat Conduction gives us the rigorous definition of one-dimensional steady state heat conduction as:

$$\frac{dQ}{dt} = -kA\frac{dT}{dx}, \text{ in Watts [W]} \tag{1.3}$$

Where,

$$k = \text{Thermal Conductivity, in } \frac{W}{m \cdot K}$$

$$A = \text{Cross-Sectional Area of Contact, in } m^2$$

$$T = \text{Average Temperature over area} A, \text{ in } K$$

$$x = \text{Distance over which heat transfer occurs, in } m$$

The negative sign accounts for the flow of heat from the hotter, more energetic, side to the cooler, less energetic, side [2]. Replacing the dT and dx with the temperatures T_1 and T_2, and thickness L, equation (1.3) becomes:

$$\frac{dQ}{dt}_{cond} = -kA\frac{T_1 - T_2}{L}, \text{ in Watts [W].} \tag{1.4}$$

This form of the equation can be rearranged to find the temperature at any point within the wall by replacing T_2 with the temperature at any given point along x, or $T(x)$, and L with any point x. Fourier's Law of Heat Conduction is easily converted into a three-dimensional vector equation by replacing $\frac{dT}{dx}$ with the gradient of temperature in the wall, or ∇T, which is equivalent to a vector with the form $(\frac{dT}{dx}\frac{dT}{dy}\frac{dT}{dz})$. This accounts for variations in temperature in all possible directions within an object, and gives the three-dimensional Fourier's Law of Heat Conduction,

$$\frac{dQ}{dt}_{cond} = -kA\nabla T, \text{ in Watts [W].} \tag{1.5}$$

To account for unsteady conduction, as is more realistic, the energy change in the wall, or $\frac{dE_{Wall}}{dt}$, will not be equal to zero. In a space environment with a significant vacuum, there will be a lack of convection, which can cause uneven heating or cooling and prevent the system from settling into a steady state. This lack of convection leaves only radiation as a (non-conductive) means of heat transfer, which tends to be slow and steady compared to convection and thus overtime these surfaces tend toward steady state temperature gradients excluding any orbital effects. This allows for the use of steady state conduction over unsteady conduction for the purposes of the work covered in this thesis.

Convection & Free Molecular Heating

Convection is a complex method of heat transfer affected by fluid mechanics and thermodynamics. It is defined simply as the transfer of heat between two bodies via a liquid or gaseous medium, however it is actually much more nuanced [27]. Due to the LEO environment of this analysis, convection is in large part neglected and thus it is deemed unnecessary to include in detail in this thesis. However, more resources can be found, and highly recommended, for this topic. An Introduction to Convective Heat Transfer Analysis by Oosthuizen & Naylor, Convective Heat Transfer by Pop & Ingham, and the Heat Transfer section of the 3rd edition of the Encyclopedia of Physical Science and Technology by George A. Greene all go into exceptional depth and detail on convective heat transfer [27] [28] [15]. There is only one fringe convective heat transfer case considered for this work, and that is free molecular heating. This effect is defined loosely above, but will be rigorously defined now. As mentioned before, in the LEO environment spacecraft will be skimming the edge of a sufficiently dense atmosphere between 200 and 450 km. Here the density is high enough for atmospheric particle impacts to occur but low enough to consider any collision to be inelastic and to make any fluid mechanics effects such as viscosity negligible. In this band, the particle collisions impart heat and thus must be considered in any LEO spacecraft temperature management system. The following table from a guide on implementing Free Molecular Heating into Thermal Desktop simulations by Eric Malroy shows the regimes at which various forms of convection dominate, and the region of interest for this work sits in the FMH regime [20].

The Knudsen number is used here to determine the regimes. It is a dimensionless coefficient defined below,

$$Kn \equiv \frac{\lambda}{L_e}, \tag{1.6}$$

General Area	Heat Transfer Mode	Relevant Environment	Description
Continuum (Kn < 0.01)	Forced Convection	Fluid flows over surface	Fluid flowing over surface results in heat transfer
	Natural Convection	Gravity environments where fluid away from surface has zero velocity	Body forces cause fluid flow near surface resulting in heat transfer
	Mixed Forced & Natural	Gravity environments where there is a flowing fluid with large temperature gradients	Both fluid flow and body forces result in an accumulated larger flow resulting in heat transfer
	Conduction	Microgravity conditions	With low gravity and cases where there is no forced flow, the fluid does not move so the heat transfers through the fluid by conduction
Mixed	Mixed Free Molecular & Continuum	Space environments with low pressure (0.01 < Kn < 0.30)	Between the continuum and free molecular mode where both modes are active
Free Molecular	Free Molecular	Space environments with low pressure (Kn > 0.3)	High temperature surface imparts energy into fluid molecules which travel to other low temperature surface, thus transferring energy. Intermolecular collisions are few while traversing the distance between the surfaces.

Figure 1.4: Modes of convective heat transfer based on Knudsen number of medium [20]

where,

$$\lambda = \text{Mean Free Path Length, in } m$$

$$L_e = \text{Effective length between impact surfaces, scale length, in } m$$

In the LEO environment, between 200 and 450 km, the average mean free path length for the dominant species of the atmosphere, atomic oxygen, is on the order of 107 m, or 100 m [12] [9]. For the purposes of this research, the spacecraft of interest is that of a CubeSat, which has a side length no larger than 36.6 cm, or 0.366 m [18]. From this an effective length can be approximated to 1 m to be inclusive of other small satellite form factors outside of

the CubeSat. With the mean path length of atomic oxygen and effective length between surfaces of the spacecraft one can estimate the Knudsen number of the LEO environment,

$$Kn = \frac{100m}{1m} = 100 > 0.3 \tag{1.7}$$

Equation (1.7) shows that the LEO environment sits within the free molecular flow regime. To rigorously define the heating expected from free molecular flow in this region, Malroy's guide to Free Molecular Heat Transfer in Thermal Desktop provides the following:

$$Q = GpF_aF_{12}A_1(T_2 - T_1), \tag{1.8}$$

Where,

$G =$ G Factor, dimensionless

$p =$ Absolute Gas Pressure, in Pa

$F_a =$ Accommodation Coefficient Factor, dimensionless

$F_{12} =$ View Factor from surface 1 to surface 2, dimensionless

$A_1 =$ Surface area of surface 1, in m

$T_{1,2} =$ Temperature of surface 1, 2 in K

Even looking at just the absolute gas pressure term informs the small magnitude of energy to be expected from free molecular flow. The area of the spacecraft surfaces and the temperature of those surfaces will be relatively small as well. The view factor represents how much of

one surface can be seen from another, and will vary between 0 and 1. The accommodation coefficient factor is similar to the emissivity coefficient factor for radiation, which will be covered more later. The Accommodation coefficient factor is dependent upon spacecraft geometry and the actual accommodation coefficient, which represents how much energy is actually transferred to a particle from a surface with a given temperature [20]. Finally, the G factor is calculated as,

$$G = \frac{\gamma + 1}{\gamma - 1} \cdot \sqrt{\frac{g_c R_u}{8\pi MW \cdot T}}, \tag{1.9}$$

Where,

$$\gamma = \text{Ratio of specific heats (based on hot surface)}$$

$$g_c = \text{Units Conversion Constant}$$

$$R_u = \text{Universal Gas Constant, in } \frac{J}{mol \cdot K}$$

$$MW = \text{Molecular Weight, in } mol$$

$$T = \text{Gas Absolute Temperature, in } K$$

Radiation

Radiation is a means of heat transfer that every massive object in the universe exhibits based on its temperature, no matter the size or geometry of the object. Most bodies, even the Earth, only radiate long wavelength, or low energy, photons in the infrared spectrum. The higher the temperature of the object, the higher the intensity and the shorter the peak wavelength of the radiation. This is known as blackbody radiation, and is well defined by

the Stefan-Boltzmann equation [24]:

$$\frac{dQ}{dt} = \sigma A(T^4 - T_c^4), \tag{1.10}$$

Where,

$$\sigma = 5.6703 \times 10^{-8} \frac{W}{m^2 K^4} = \text{Stefan-Boltzmann Constant}$$

$$A = \text{Area of emitting surface, in } m$$

$$T = \text{Temperature of the emitter, in } K$$

$$T_C = \text{Temperature of the environment, in } K$$

$$\frac{dQ}{dt} = P = \text{Thermal Power}$$

Not all bodies or objects are perfect blackbody emitters, however. Where a blackbody emitter absorbs and emits one hundred percent of the energy in a closed system, reflected and transmitting no energy. A gray body emitter absorbs, emits, reflects and transmits some percentage of that energy within the closed system. This inefficiency is accounted for by the emissivity term, , added into the Stefan-Boltzmann Equation, as shown below [24],

$$\frac{dQ}{dt} = \varepsilon\sigma A(T^4 - T_c^4), \tag{1.11}$$

Where,

$$\varepsilon = \text{Emissivity of the radiating surface, dimensionless}$$

This term defines how much energy an object radiates for a given temperature, size and shape as compared to that of a perfect blackbody emitter, or when =1. The smaller the emissivity, the less energy that is radiated out as photons. Additionally, the total energy incident on a surface must be evenly split between being absorbed, transmitted or reflected, as seen below,

$$\alpha + \rho + \tau = 1, \tag{1.12}$$

Where,

$$\alpha = \text{Absorptivity, } 0 < \alpha < 1$$

$$\rho = \text{Reflectivity, } 0 < \rho < 1$$

$$\tau = \text{Transmissivity, } 0 < \tau < 1$$

For an opaque surface, such as an aluminum panel for a spacecraft, the transmittance is canceled out, reducing equation (1.12) to,

$$\alpha + \rho = 1, \tag{1.13}$$

This is a consequence of conservation of energy, and impacts the energy balance of each surface of a spacecraft, along with emissivity.

Combining all three of the aforementioned heat transfer methods: conduction, the free molecular flow regime of convection, and radiation, the primary mechanisms for temperature management emerge. A spacecraft can be fitted with straps, heat sinks, radiators and

heaters to form a closed loop control system that relies on deep space as a heat sink and the spacecraft as a heat source. To facilitate a system such as this, there are a number of technologies and design methodologies that have evolved with the CubeSat standard, which will be covered in detail later.

1.2 EMCCDs

The goal of this project is to design a temperature management system for a novel Electron Multiplying Charge-Coupled Device (EMCCD) camera system for astronomy applications. This new technology is developed by a Canadian company called Nüvü Camēras and is an advancement on the Charge-Coupled Device (CCD) technology developed by George E. Smith and Willard S. Boyle in 1969 [4]. These CCDs work by using a photosensitive layer of silicon to receive photons that are then converted into electrons via the photoelectric effect. These photoelectrons are then collected into a bank of capacitors corresponding with a pixel at or near the location of impact. A shift register, or control circuit, drives these capacitors to move their electrons through the image array and into a storage array before being processed by a charge amplifier. This amplifier converts the electrons into a sequence of voltages which is then sampled, digitized and readout as an image stored in memory [4]. The EMCCD developed by Nüvü Camēras functions in the same way but adds in a multiplication stage between the storage array and readout stage, as seen below in Figure 1.6 [6].

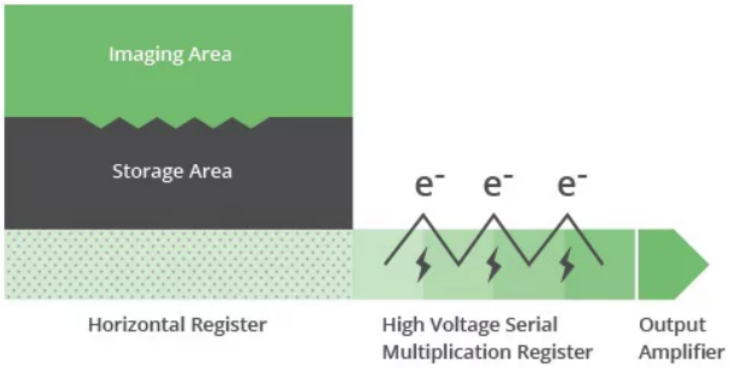

Figure 1.5: EMCCD High Level Functional Diagram [6]

Electrons from the storage array are pushed pixel by pixel through a series of high voltage electrodes that offer a one to two percent chance of generating a second electron by impact ionization, which can result in a single electron cascading into thousands before reaching the output amplifier stage [6]. This novel design allows for extreme low-light imaging and even photon counting capabilities. However, this performance comes with operational challenges. These challenges include readout noise, electron multiplication gain damage, clock-induced charges, charge transfer efficiency, excess noise factors, and most importantly for this project, thermal noise.

Readout noise is typically on the order of two to ten electrons per operation and occurs during the output amplification stage when charges are amplified and digitized. In high-illumination situations, such as when there are thousands of electrons per pixel, this noise is negligible. Due to the multiplication register of EMCCDs, this noise will always be negligible when operating in photon counting mode [6].

The electron multiplication stage is sensitive to saturation and premature aging and damage because of this. This stage boosts not only the desired signal, but also any electrons produced prior to the stage by means other than photons. These electrons can come from random

excitation due to thermal energy or clock-induced charges, and the best way to minimize this risk is to take steps to reduce production of these excess electrons [6].

Clock-induced charges are generated by the signal that drives the movement of electrons from the image array into the storage array, and from the storage array into the multiplication stage. Typically a high readout rate is desired for cameras as this maximizes the number of images that you can acquire for a given amount of time. However, moving the charges at such a rate requires a high voltage and high frequency driving signal, and as the frequency increases so does the excess electron noise. This can be dampened by creating finer, or smaller width, and more adjustable driving signals [6].

During the movement of charges between arrays and through the stages, some electrons can be left behind, especially at high readout speeds. The charge-transfer efficiency is how this phenomenon is defined for a given detector system. The less electrons that are left behind after a transfer, the more efficient the system will be and the less noise that is left behind to decrease image quality for the next pixels [6]. An example of the reduction in quality can be seen in the figure below as an artificially brighter image on other EMCCD systems due to poor charge transfer efficiency.

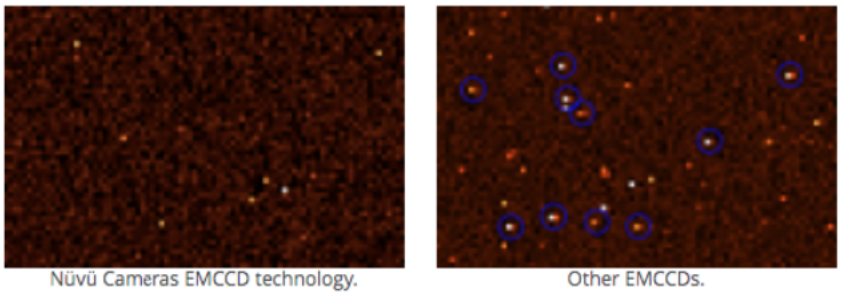

Figure 1.6: Charge Transfer Efficiency of Nüvü Camēras EMCCD vs. other EMCCDs [6]

The avalanche process within the electron multiplication stage is unpredictable by nature. The amount of electrons that entered the multiplication stage can never be exactly calculated

from the output signal. Only the mean gain of the output signal can be found, as the signal follows a Poisson distribution as seen below in Figure 1.8 [6].

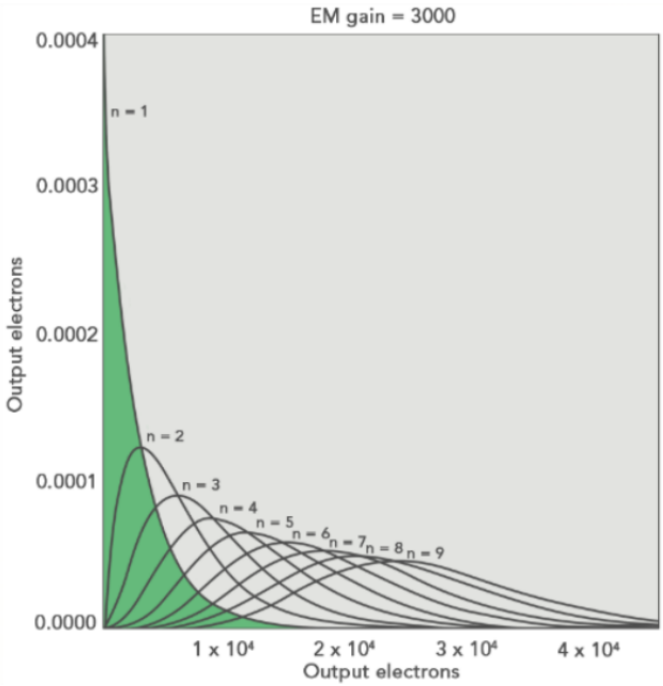

Figure 1.7: Poisson distribution of a mean EM gain of 3000 for the output probability distribution plotted against the number of output electrons for n input electrons [6]

As seen above, the electron distributions overlap significantly no matter the number of electrons, n, which makes it impossible to determine the exact number of input electrons. This uncertainty introduces a noise factor with a value of 2 at high electron multiplication gain. This noise source is stochastic in nature and is most noticeable in low light conditions. It affects the signal to noise ratio of the detector as if its quantum efficiency, or probability of converting a photon into an electron, was cut in half. EMCCDs in photon counting mode reduce the magnitude of this effect by counting the number of photoelectrons in a pixel and giving each a measurement of one or zero prior to the charge amplification register. Therefore, the charge amplification register does not even get the chance to apply this uncertainty to the measurement [6].

Thermal noise is defined as a temperature dependent electron source within the detector that will always be active, even when not exposed to photons. The particles within the silicon array all have energy based on their temperature, and even this is enough to release electrons into the array that get caught in the potential well of a pixel. This effect is most noticeable on dark frames and will even arise in complete darkness, hence why it is known as dark current. The only solution to dark current, and the one relevant to this project, is to cool the detector down to temperatures low enough to meet a noise tolerance set by the designer. The following figure shows the temperature dependence of electron noise in a CCD detector [22].

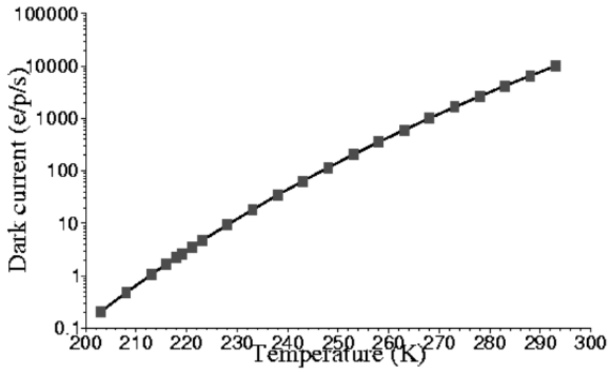

Figure 1.8: Electron noise per pixel per second versus the temperature of the detector [22]

In order to achieve a dark current value of less than 1 electron per pixel per second, the entire detector should be cooled down to less than 214 K. The Nüvü Camēras EMCCD is typically cooled to -85℃, or 188.15 K, which allows for a dark current value less than 0.1 electron per pixel per second. This project will focus on controlling thermal noise by manipulating the temperature of a Nüvü Camēras EMCCD detector and controller.

1.3 CubeSats

The Nancy Grace Roman Space Telescope has base lined the CCD201-20 EMCCD detector by Teledyne e2v along with custom controller electronics from Nüvü Camēras for its Coronagraph Instrument [7]. The following figure from Nüvü Camēras paper on the development of the EMCCD payload for the NASA Jet Propulsion Lab (JPL) coronagraph instrument.

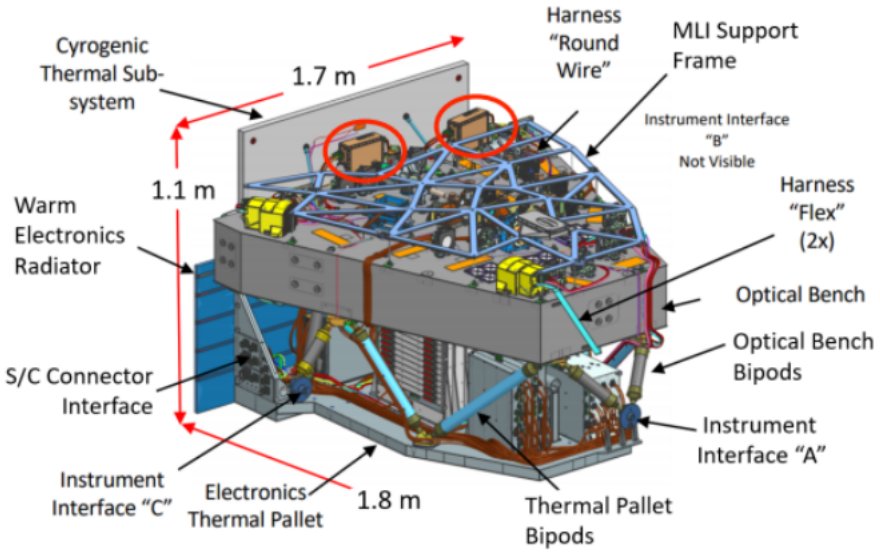

Figure 1.9: JPL Nancy Grace Roman Coronagraph Instrument mechanical layout [7]

From Figure 1.10, the scale of the instrument is obvious. The full instrument measures in the meters and has a large volume for cable routing, lens placement, and thermal systems. This project focused on a payload size much smaller than the development budget than the Nancy Grace Roman space telescope had. Instead, the objective of this project was to iterate on the Nüvü Camēras EMCCD controller design as well as the Teledyne e2v CCD201-20 detector for a 6U CubeSat form factor, which is on the scale of centimeters.

The CubeSat form factor is a standard chassis design based on shape, size, deployer, mass and electrical requirements developed by California Polytechnic State University in 1999 [13]. The chassis is standardized in a unit called the U, where 1U has the maximum external

dimensions of 113mm by 100mm by 100mm, and all progressions beyond or below that can be characterized as stacked or half 1U's. For instance, a 2U CubeSat is simply the measurement equivalent of two stacked 1U's, giving dimensions as seen below in Figures 1.11 and 1.12 [18].

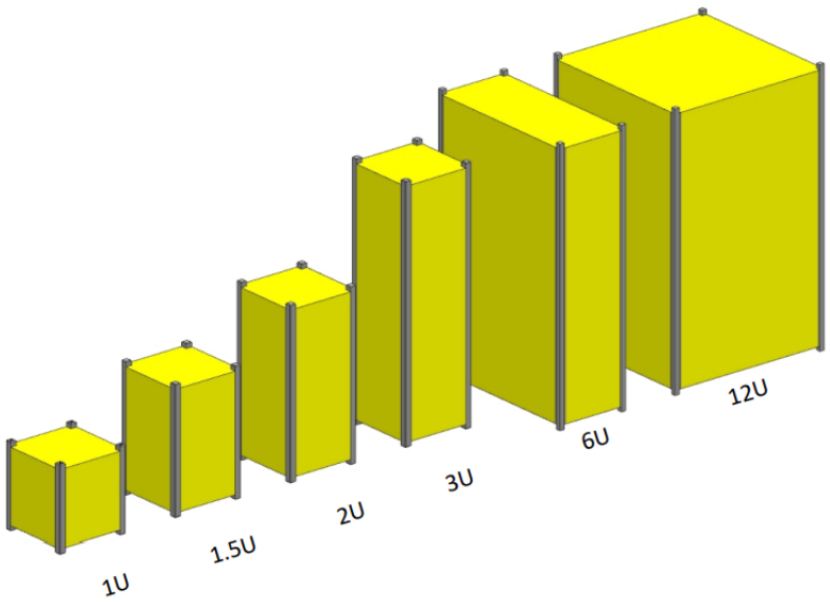

Figure 1.10: The Current CubeSat family, 1U - 12U [18]

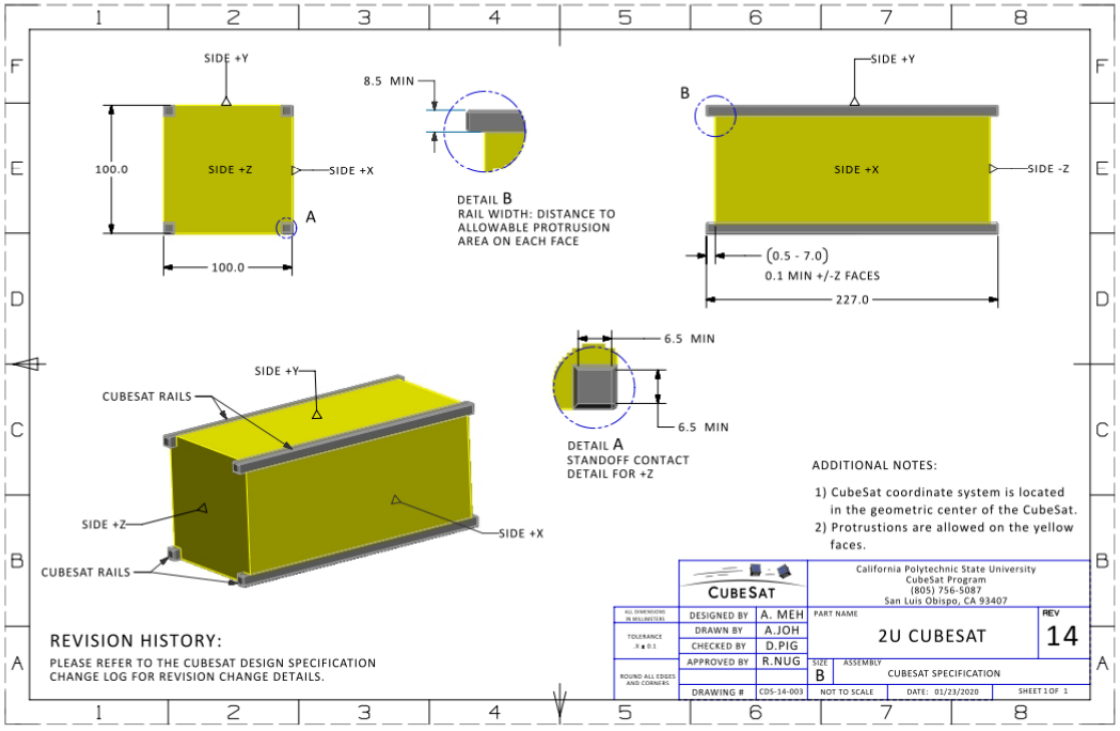

Figure 1.11: External dimensions of a 2U CubeSat [18]

The small form factor when compared to flagship space telescopes and other large spacecraft chassis creates challenges for the management of temperature sensitive payloads. CubeSats suffer from the following thermal challenges [5]:

Table 7-1: SmallSat Thermal Control Challenges

SmallSat Property	Challenge
Low thermal mass	The spacecraft is more reactive to changing thermal environments.
Limited external surface area	There is less real estate to be allocated to solar cells, designated radiator area, and/or viewports required for science instruments.
Limited volume	There is less space for electronic components, science instruments, and thermal control hardware. Components can be more thermally coupled and it can be harder to isolate different thermal zones.
Limited power	There is less power available for powered thermal control technology.
Power Density	There is a big challenge to dissipate power as electronics are stacked close to each other, sometimes with no direct path to radiator.
MLI Edge Effects	MLI can "short" along the edges resulting in degraded performance, not specific to SmallSats; more of a general spacecraft issue.

Figure 1.12: SmallSat Thermal Management Challenges [5]

1.3.1 Project Requirements

With these challenges in mind, the objective of this project is to meet the following thermal system requirements [8]:

Table 1.4: Nüvü Camēras EMCCD Thermal System Requirements [8]

Mass	$< 3kg$
Power Consumption	$\leq 10W$
Volume	$10cm$ x $10cm$ x $10cm$
Cooling Method	100% Passive
Environment	Vacuum
Electronics Temp. Range (Non-Op)	$-40°C$ to $+60°C$
Electronics Temp. Range (Operational)	$-35°C$ to $+60°C$
EMCCD Temp. Range (Non-Op)	$-150°C$ to $+125°C$
EMCCD Temp. Range (Operational)	$-135°C$ to $+60°C$
EMCCD Temp. Range (Performance)	$-110°C$ to $-85°C \pm 0.1°C$
Radiation Environment	Low Earth Orbit

The EMCCD performance temperature resolution is based on commercially available, ground based versions of Nüvü Camēras' EMCCD, and was deemed too challenging for the CubeSat form factor after modeling, so this was changed to a resolution of ± 0.25℃.

Chapter 2

Simulation Tools

2.1 Modeling and Simulation Software

2.1.1 Thermal Desktop and Autodesk Inventor Overview

To go about the work of designing a thermal system, two categories of software were necessary: 3D Computer Aided Design (CAD) modeling software and thermal simulation software. CAD models of relevant components from Nüvü Camēras were to be used as references for the 3D modeling of the system, and thermal simulation software is used to perform calculations with greater efficiency and fidelity than a human could. There are many options available for both of these categories, with the most popular CAD programs being Dassault Systemes' Solidworks, Autodesk Inventor, Autodesk TinkerCAD, FreeCAD, Creo, Siemens NX, Rhino, and Autodesk Fusion 360. This list is non-exhaustive, and of these, Solidworks, Inventor, and Siemens NX are considered professional modeling programs with heritage throughout the industry. All of these programs provide a full suite of mechanical design features that allow for the creation and manipulation of any geometry necessary for designing the system. However, the professional programs provide additional environments for testing of designs, such as stress analyses. Thermal simulation programs are similarly prolific to 3D modeling programs, with options like Ansys Lumerical HEAT, STK SOLIS, Star-CCM+, Thermal Desktop, Siemens NX, MSC Nastran, and OpenFoam. However, the capabilities and forms

that these programs take vary. Software like STK SOLIS, Thermal Desktop and Siemens NX are built into or apart of other software. For example, STK SOLIS is an additional feature for the mission planning software, Systems Tool Kit (STK), that allows for the calculation of environmental thermal effects on spacecraft. Thermal Desktop is built into the framework of Autodesk AutoCAD, a primarily 2D modeling program that can handle 3D geometry, and allows for the in-situ creation or importation of custom geometry for thermal analysis. Some of this software is free and open-source, such as OpenFoam, which makes it easy to access.

This project requires a smooth pipeline that allows for the creation of geometry in a modeling program and movement of those models into thermal analysis software, as well as an efficient process for modifying geometry and reanalyzing in a short time frame. A key additional requirement is native support of the orbital environment, i.e. the inclusion of the Sun and the Earth as heat loads, as opposed to forcing the environment in via assumptions and hand written heat loads. The dynamics of the orbital environment must also be accounted for to provide for accurate simulations of a spacecraft in Earth orbit. Finally, the program must provide high fidelity thermal analysis capabilities down to the component level, i.e. the program must give accurate steady-state and transient behavior from the smallest bolt up to the largest surface, all within an orbital environment. Programs such as OpenFoam, Ansys Lumerical HEAT and Autodesk CFD provide the detailed component focus that is necessary, but does not natively support the orbital environment or the dynamics necessary for this project. Programs such as STK SOLIS, Star-CCM+ and Thermal Desktop provide both the spacecraft focus and the orbital environment support necessary, but Thermal Desktop stands out above SOLIS and Star-CCM+. Thermal Desktop provides high-fidelity steady-state and transient results based on the quality of the geometry mesh and includes an add-on called RadCAD that provides native support of orbital dynamics and the orbital environment. It is built into Autodesk AutoCAD, which provides the ability to create custom geometry and

meshes as well as to import geometry from other modeling programs, with emphasis on other Autodesk modeling software.

To match Thermal Desktop's analysis capabilities, Autodesk Inventor Professional was chosen for modeling work. Both the team at Nüvü Camēras and Virginia Tech have years of experience with the program, and the synergy between Thermal Desktop's integration into Autodesk AutoCAD and Inventor allowed for easy 3D model creation and importation for thermal analysis. The following figure shows the user interfaces of both Autodesk Inventor and Thermal Desktop with the same test component.

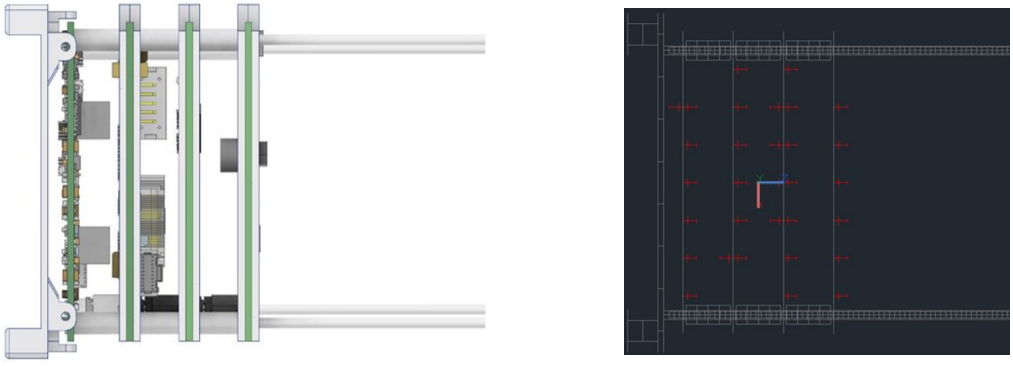

(a) Camera Controller in Inventor (b) Camera Controller in Thermal Desktop

Figure 2.1: EMCCD Camera Controller in both Autodesk Inventor and Thermal Desktop

The complicated and dense geometry built within Autodesk Inventor allows for an accurate mechanical design reference, which will aid in building a physical prototype in the future. However, simulations within Thermal Desktop tend to take longer to run as the complexity of the geometry is increased so the model is simplified for thermal analysis. The Inventor model is imported and turned into a skeleton for a mesh to be created over top of it, and the nodes and elements of this mesh are then modified to suit each analysis run. These modifications include defining the conductivity, specific heat, density, surface reflectivity, absorptivity, and emissivity, along with some thermoelectric and stress properties.

2.1.2 Thermal Desktop Heritage and Advantages

Thermal Desktop is a software package developed by Cullimore & Ring Technologies, and is built into the framework of Autodesk AutoCAD. It has a deep heritage with many NASA projects and is well documented within the NASA SSRI Knowledge Base for Thermal Analysis [23], and was recently acquired by Ansys. Thermo-optical and thermophysical properties can be defined for custom materials, and it contains a library of pre-made materials for easy use as well. The user can define a very dense or loose mesh for geometry and define the conduction properties for each node and element in that mesh.

The RadCAD add-on allows for the definition of an orbit around a customizable central body and the corresponding direct solar, planetary IR and albedo flux. The typical setup is with Earth as the central body, as seen below, with a corresponding orbital track. This orbital track can be broken into as many analysis points as desired. At each point any user defined thermal analysis cases are run, be it a steady-state or transient behavior check.

As seen above, RadCAD also allows for the definition of spacecraft orientation over time in an orbit, orbit analysis positions, central body data, albedo, solar, and planetary IR flux, as well as the application of a spin on the spacecraft.

Given the experience that both teams have with Autodesk products, the documentation available, and breadth of features that fit the project requirements, Thermal Desktop was the selected software for analysis.

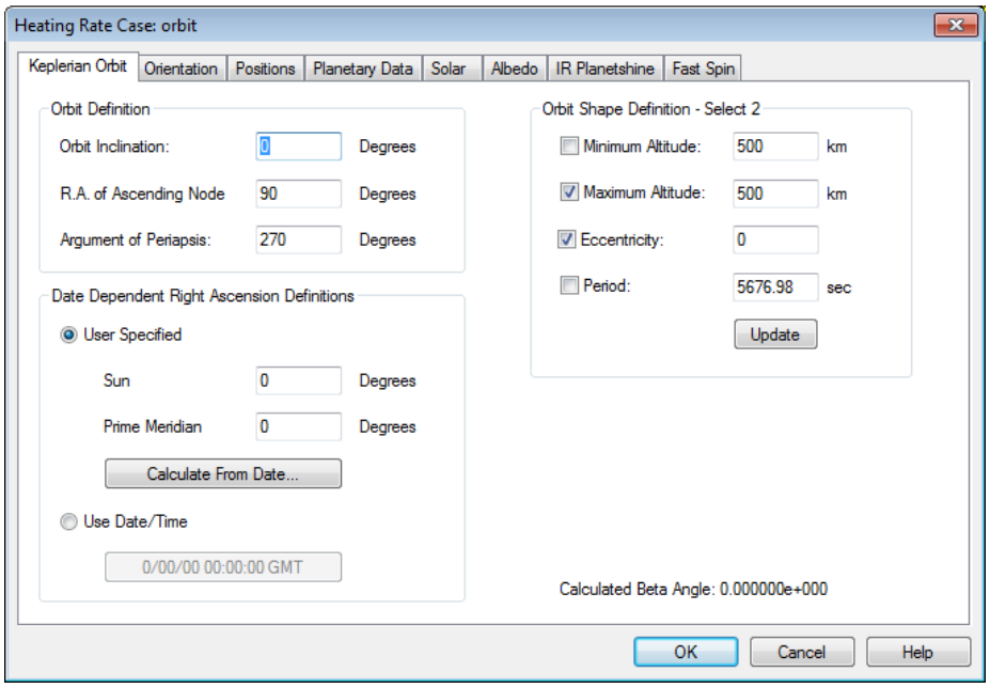

Figure 2.2: RadCAD Editing Screen for a Keplerian Orbit

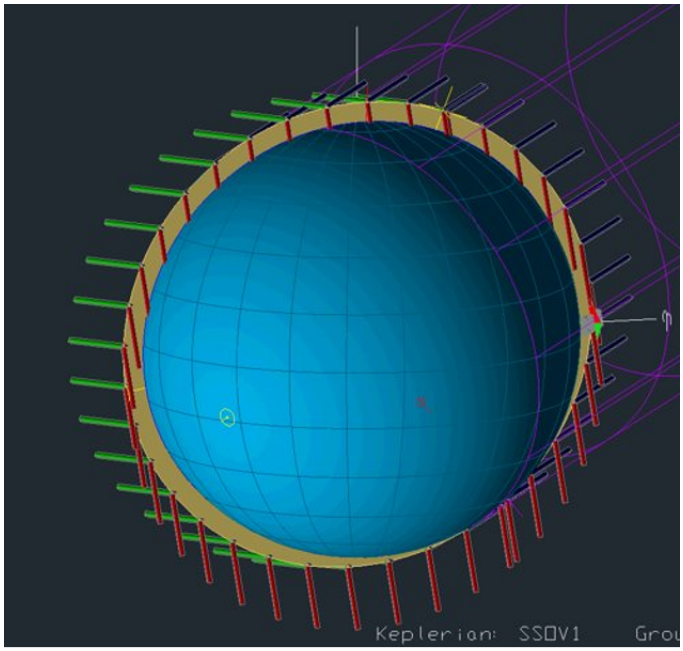

Figure 2.3: RadCAD Orbit View of a LEO Track

Chapter 3

System Modeling

To achieve the goal of this project multiple objectives were laid out: create 3D models within a CAD program for desired control system, import CAD models of the system into a thermal analysis program, run transient and steady-state analyses to determine behavior, update CAD models based on analysis results, and repeat until a system is found that sufficiently meets the design requirements. A large portion of these objectives can be defined as system modeling, and the process requires definition of environmental loads, system loads, and any assumptions. Primary concerns for this system include the characteristics of an example orbit, expected environmental heat loads, spacecraft orientation information, system heat loads, system interfacing with the rest of the spacecraft, and other necessary assumptions for analysis.

3.1 Simulation Details and Assumptions

3.1.1 Orbit Characteristics

Even though the goal of this project was to design a subsystem for a payload, there are many aspects of a parent spacecraft that must be considered. This payload will potentially see flight on a wide array of CubeSat spacecraft that will have their own missions, requirements and orbits. An objective of this design is to allow for a broad range of missions and applications,

and as such a general orbit must be chosen for analysis. An exemplar orbit was chosen between the teams at Virginia Tech and Nüvü Camēras. This orbit is defined below in the following table:

Table 3.1: Model Orbit Characteristics

Orbit Characteristics (Keplerian)	
Element	Value
Eccentricity	0.00000
Altitude (km)	600.000
Inclination (°)	97.9400
Period (s)	5801.23
R.A. of Ascending Node (°)	0.00000
Argument of Periapsis (°)	0.00000

These characteristics are defined within RadCAD via the editor depicted in Figure 2.2 and results in an orbital track like the one shown in Figure 3.1 below.

3.1.2 Pointing Cases and Environmental Heat Loads

Steady state and transient simulations of the system were modeled in three cases with corresponding environmental heat loads and spacecraft orientations: a cold, warm, and hot case.

These heat loads correspond both to the pointing constraints for each control chain and the temperature of boundary nodes on the corners of the detector headboard. In the Cold case, nodes are kept at a temperature of 253.15 Kelvin, or -20°C, representing the controller tem-

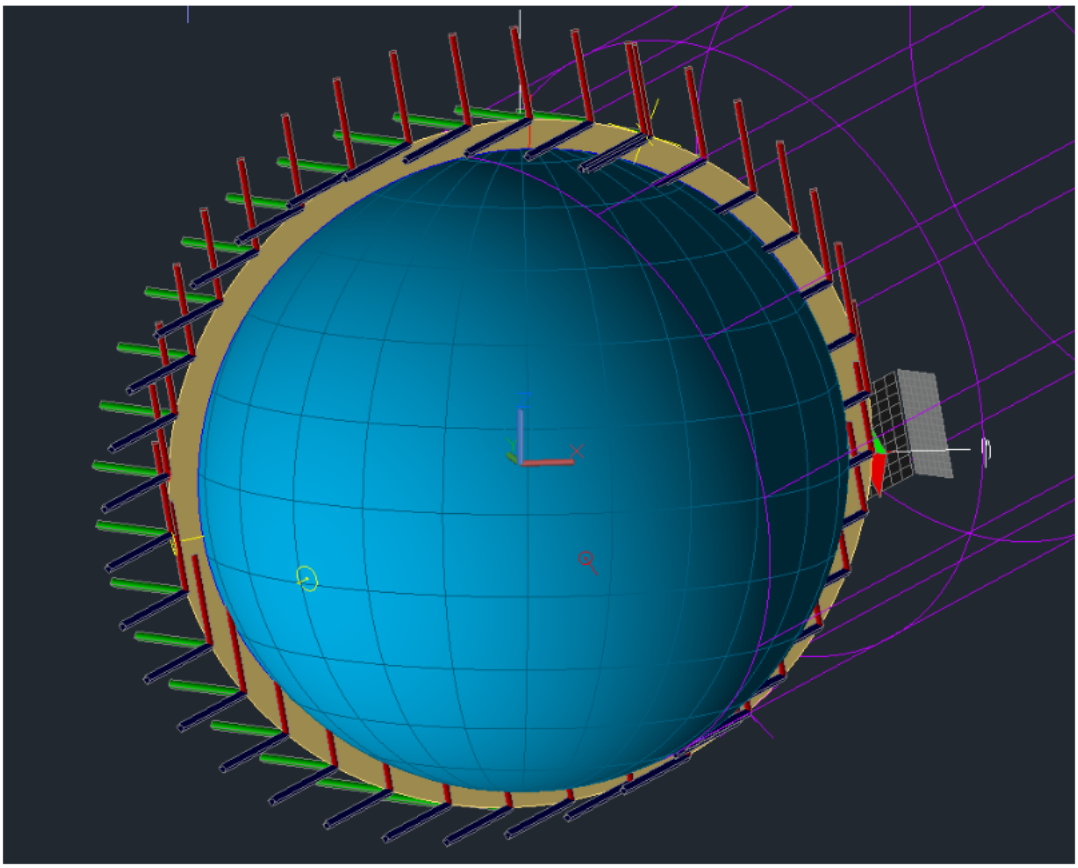

Figure 3.1: Thermal Desktop Visualization of the desired sun synchronous orbit for the cold pointing case

perature and its conduction through the chassis rails. Figure 3.2 below shows the controller and detector models for this configuration. In the Cold case, the -Z axis of the spacecraft is always in-line with the solar vector. This keeps the 6U faces that contain the radiators shaded at all times, removing direct solar exposure as a heat load. It is important to note that both albedo and planetary IR exposure are still present and must be accounted for. In reality this kind of precise pointing control is challenging to achieve, but for this project a perfect attitude control system is assumed.

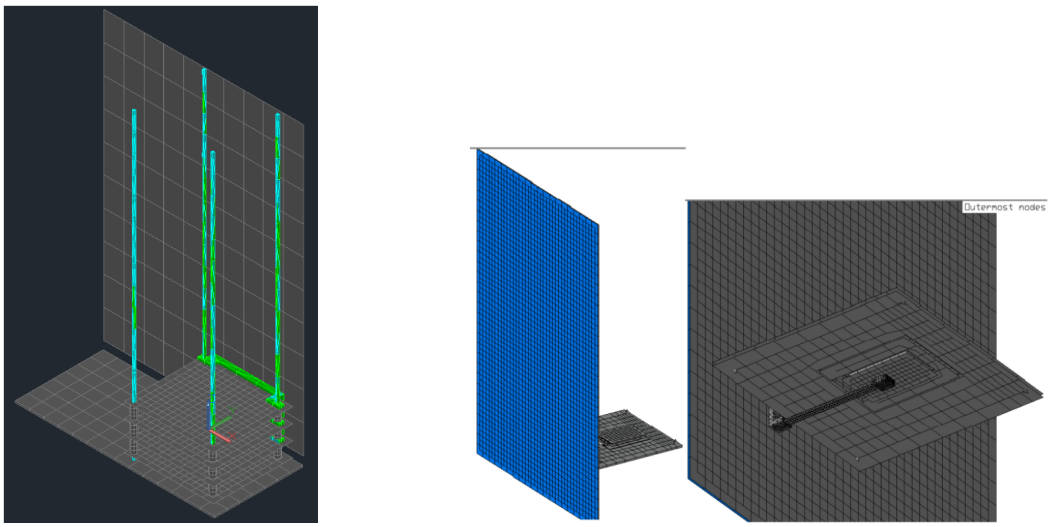

(a) Isometric view of Controller Chain mesh (b) Isometric views of the Detector Chain mesh

Figure 3.2: Controller and Detector Meshes in Thermal Desktop

In the Warm and Hot cases, nodes are kept at 273.15 Kelvin and 293.15 Kelvin respectively, corresponding to 0°C and 20°C. Every other node in the headboard, detector, heat sink and thermal strap are given an initial temperature of 188.15 Kelvin, or -85°C, corresponding to the nominal operating temperature of the detector. This initial state carries the assumption that the system is already operating and has reached a steady state in the desired temperature range. For the Warm case, the +Z axis of the spacecraft is aligned with the velocity vector while the -Y axis (radiator face) is aligned Nadir, or always facing the Earth. This introduces the possibility for direct solar exposure on the radiator and constant exposure to albedo and planetary IR flux on the cryo-chain radiator. For the Hot case, the -Y axis of the spacecraft, or the cryo-chain radiator face, is always aligned with the Sun, presenting the highest direct solar exposure load while also allowing for albedo and planetary IR exposure.

Two versions of these simulations were completed, one with no active input into the system, simply allowing the system to converge to a steady state solution, and the second with the input of a 0.5W and 1W resistive heater into the heat sink. The coldest result of these steady

state simulations were then used as an input to a transient solution as an initial cold case for the time dependent heater response.

Note for these simulations, the detector chain includes the following components: the EM-CCD detector, the headboard on which the detector is mounted, the heat sink, thermal strap and radiator, as shown below in Figure 3.3. Each component within this conduction chain is assumed to have a thermal epoxy interface to fill any surface imperfections and improve thermal conductance. As detailed previously, this epoxy (Masterbond EP37-3FLFAO) provides a thermal conductivity of $1.44\frac{W}{m\cdot K}$, a specific heat of $1,110\frac{J}{kg\cdot K}$ and density of $1,100\frac{kg}{m^3}$ and serves as a thermal interface that aids in smoothing out surface roughness to improve conductance, and in fastening each component in the chain, without being too rigid and impacting vibration performance significantly [21].

Each metal component in the detector chain is Aluminum 6061 with a thermal conductivity of ~$237\frac{W}{m\cdot K}$ at -85°C. Although most often negligible, having a consistent medium for heat transfer helps prevent transient effects that could reduce the efficiency of the system. Aluminum was chosen over the more conductive copper, graphite, or graphene thermal straps because of how cheap it was at the time of design Testing each material within the thermal strap has shown that the dimensions of the thermal strap are already so small as to not feasibly be manufactured with any material of higher conductivity.

3.1.3 System Heat Loads and Assumptions

The steady-state simulations for the controller chain include the four PCBs that make up the controller itself, the spacers, radiator interface clamps, -Z chassis stand-in panel, and the radiator. The model includes the expected heat loads for each board, ordered from top to bottom as seen in Table 6:

Table 3.2: Expected Internal Thermal Load

Board	Total Heat Expected (W)
CCD Drive	3.0905
Vertical Drive	3.692
Digital	3.56
Power	2.25
Total	12.5925

The controller has similar operating temperatures to the supporting electronics of the spacecraft, so it would be beneficial to share the radiator with these components assuming there is a large enough cooling capacity. In this case, an additional constant heat load is placed on the radiator to account for the supporting electronics. This heat load is set to 10W, a typical operating power consumption for supporting electronics including an Electrical Power System (EPS), on-board computer (OBC), battery pack, Attitude Determination and Control System (ADCS) unit and radios, for one case. As a worst-case scenario, this heat load is increased to 20 W in the final steady state simulation. In total, the expected internal load as a worst-case scenario approaches 32.5925 W, which according to preliminary environmental heat load simulations in MATLAB shown in Figure 3.3 below is still within range for a cold-biased passive system.

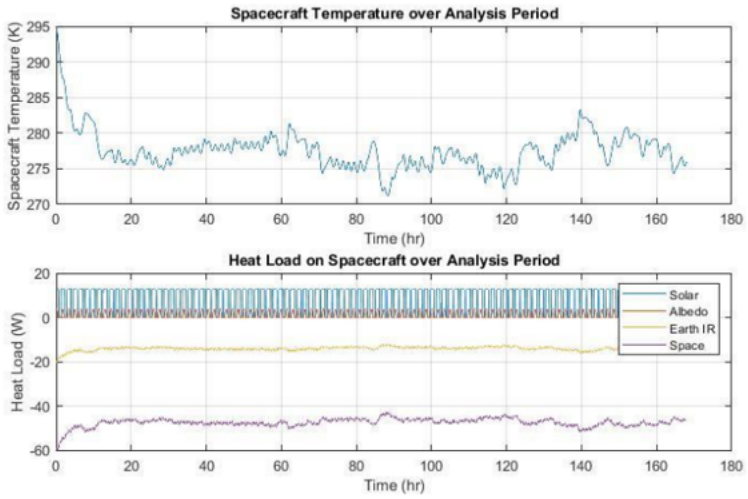

Figure 3.3: Shoebox Model Spacecraft Temperature and Loads in SSO (Altitude 600km, Ecc.: 0, Inc.: 97.94°) over 1 week

3.1.4 System Interfacing and Design

To meet the thermal requirements for this payload the first step was to make sure that the temperature range of interest could be achieved, and ideally even colder, with an entirely passive system. This is not a guarantee in LEO, as direct solar, albedo and Earthshine effects can be a major impactor depending on the characteristics of the orbit. Seeing as the aim was for 0.4W of heat dissipation and a steady state temperature of -85±0.25°C for the detector, Figure 3.4 below shows that both radiators and thermoelectric coolers satisfy these constraints. Given that a passive system is preferred and Figure 3.4 shows the performance range for radiators as appropriate, they were chosen for a cold-biased, fully passive control system for both the controller and detector. The detector chain will consist of an external radiator, an Aluminum 6061 thermal strap, a heat sink with resistive film heater, and Masterbond EP37-3FLFAO thermal epoxy in between each contact interface.

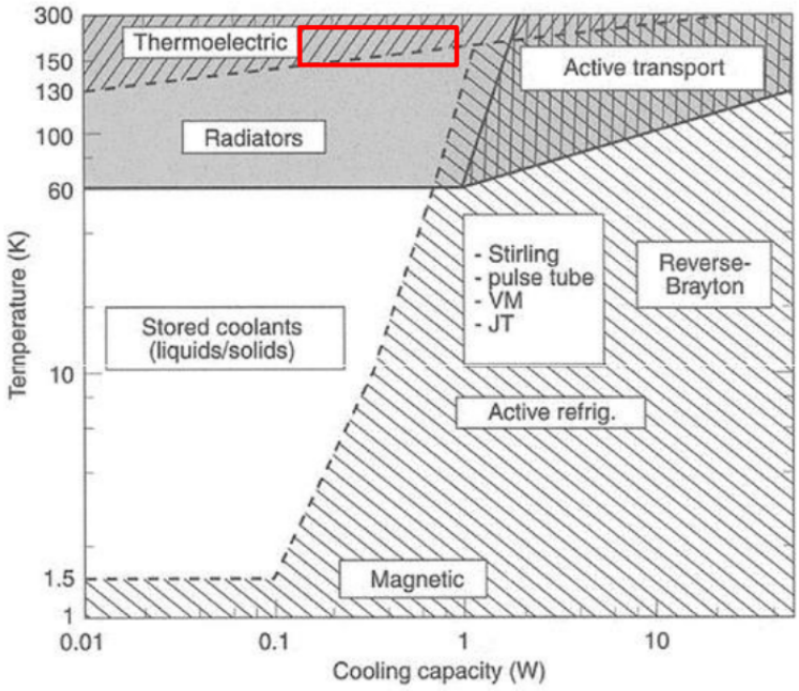

Figure 3.4: Thermal Control Regime by Temperature and Cooling Capacity

As discussed earlier, the 3D CAD program Autodesk Inventor 2022 was used for designing and assembling reference assemblies. For the purposes of this project, 3D models of the system were built within Inventor and exported thereafter to Thermal Desktop for meshing and further processing before simulation. The following is a series of renders from Inventor of the full system, both within and without the example 6U CubeSat.

Figure 3.5 below illustrates the full CAD assembly, where Figure 3.5 (right, bottom) shows a spacecraft render containing supporting components in the right-most 3U of the 6U bus. This is also shown in the top compartment of Fig. 3.6 (left). These are the ADCS, an S-Band Transceiver, the EPS and Batteries, a UHF Transceiver, and an OBC.

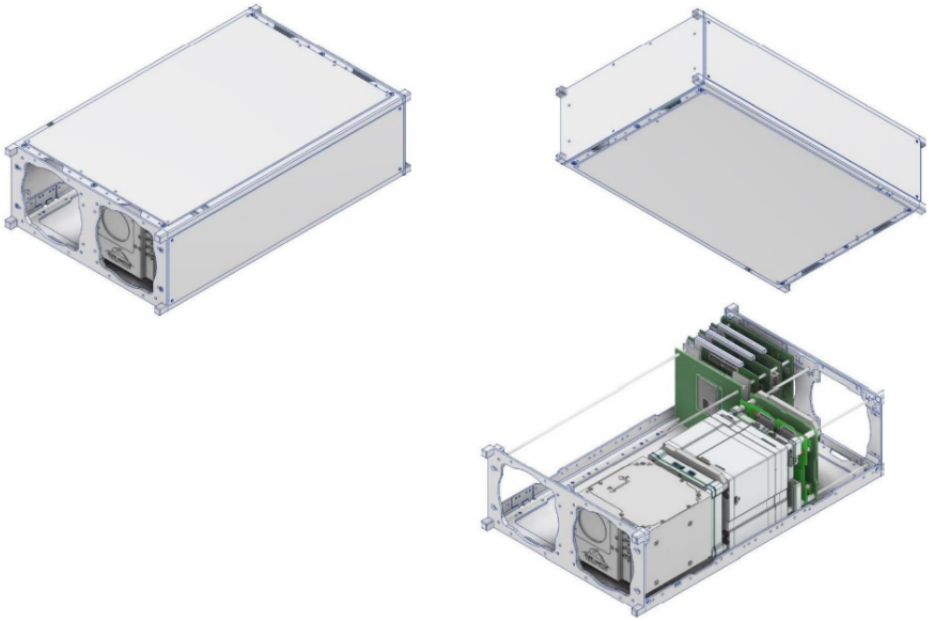

Figure 3.5: Example 6U Spacecraft with Nüvü Camēras EMCCD Integrated

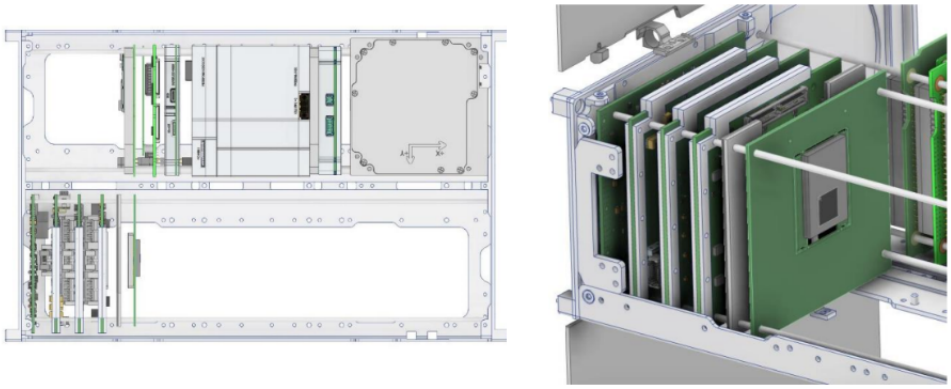

Figure 3.6: (Left) Top-Down view, (Right) Close-Extent ISO view of the EMCCD payload

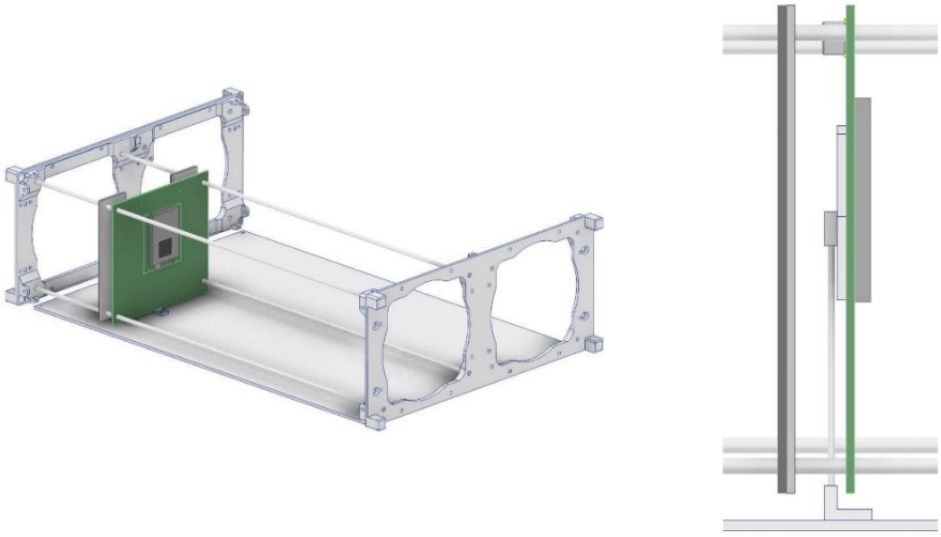

Figure 3.7: (Left) Full view of all directly connected Detector Chain components (Right) Close-up of the headboard, thermal strap, and IR shield

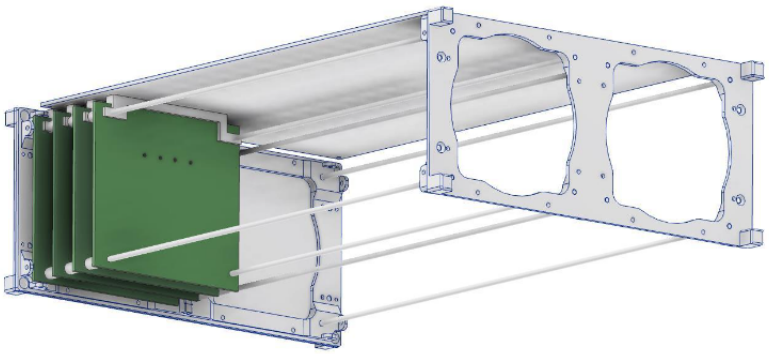

Figure 3.8: Controller Chain visible in the back left of the 6U chassis

Above the OBC in this stack sits the interface board between these parts and the Nuvu EMCCD controller. The top left corner shows the 1U compartment that contains the Nuvu EMCCD controller and headboard integrated with the rails, as well as the management system.

Figure 3.6 (right) zooms into this section, and the bottom compartment in Figure 3.6 (left) shows a view from the top. These renders capture the combined controller and detector

components in a 1U configuration, which was an important design decision to allow for integration into a more diverse range of CubeSat chassis. This work has seen these two chains (detector and controller) separated into different thermal systems for analysis. Additional details can be seen in Figure 3.7 and Fig. 3.8.

The detector chain is the primary focus for this project due to the extreme temperature constraint. The thermal stability of the sensor is considered to be the highest risk item and the flight electronics to be of low design risk. To reach the nominal operating temperature of -85°C (188.15 K) ± 0.25°C, the design utilizes an Aluminum 6061 heat sink. The detector is directly fastened to this heat sink through a thermal epoxy interface. For a thermal epoxy, Masterbond EP37-3FLFAO will be used as the thermal interface for every component from the detector to the radiator in the chain. It will act to fill any surface roughness and improve the heat transfer efficiency of the system [21]. The heat sink is connected to an Aluminum 6061 braided cable thermal strap designed with a conductance of $0.00523\frac{W}{K}$, which is tuned to dissipate $400mW$ at -85°C (188.15 K). The thermal strap is connected to an Aluminum 6061 radiator panel with an area, $A = 0.06m^2$ and an AZ93 White Paint coating, corresponding to one panel of a 6U CubeSat [34].

The radiator was designed to balance the heat generated by the spacecraft and environment with the cooling capacity of the 6U panel such that the required input power to the resistive heater is minimized. This corresponds to ~0.5 W of output, which would place the radiator area $A_{ideal} = 0.01103 \cdot m^2$. This calculation does not capture heat loads such as albedo reflective effects and IR radiation from the central body in orbit. However, from previous flight programs which provided useful thermal data in LEO (at 400-500 km), expectations are to maximize radiator area and design highly efficient spacecraft pointing requirements that place each 6U face in as constant a shade state as possible.

One of the most significant challenges in the design is the large difference in temperature

between the detector and the controller. The controller is not constrained to -85°C (188.15 K) and instead has an operating range between -20°C (253.15 K) and 20°C (293.15 K). This is a temperature difference of 65°C to 105°C (65 K to 105 K) at 20 mm separation. Although it is not necessary to consider the otherwise significant effects of convection in a space this small (due to operating in space), this temperature difference still constitutes a large infrared (IR) radiative heat load from the controller to the detector headboard and other components of the detector chain. Thus, to prevent this load from interfering with detector thermal stability, an IR shield of coated Aluminum 6061 is included between the controller stack and the detector and headboard. The controller side of the shield is coated for an emissivity and absorptance of 0.91 and 0.15 with AZ-93 White Paint, respectively, while the detector side will be buffed aluminum, providing an emissivity of 0.03 [34]. An important note for this system is that both the detector and controller chains are thermally coupled through the chassis rails. This is done to allow for the headboard and controller to dissipate through the chassis, essentially adding the spacecraft chassis as an additional heat sink.

The headboard is designed to isolate the detector where an inner mount face is cut into the headboard, with 4 bridges connecting the two faces. These 4 bridges, visible in Figure 3.11 (left), provide a total conductance of $G_{bridges} = 1.2 \cdot \frac{mW}{K}$ into the inner mount for the detector. The detector is thermally coupled to the inner mount via thirty $50\mu m$ Constantan wires that provide a total conductance of $G_{wires} = 0.25 \cdot \frac{mW}{K}$, providing effective insulation from the headboard.

The controller chain is a completely separate system to the detector chain aside from the coupled connection in the chassis rails (which is mitigated as above via the thermal strap). As shown in Figure 3.8, the controller is clamped by Aluminum 6061 heat sinks that are in direct contact with the chassis rails. This design was used in previous programs at Virginia

Tech and therefore has some heritage. Full simulation of the controller chain in Thermal Desktop has shown that no extra surface area was necessary and that sufficient heat can be dissipated through these clamps.

The clamping heat sinks have been designed to fit the available surface area for conduction pathways on each board and provide contact with the chassis rails and the dedicated radiator for the chain. The radiator-clamp interfaces for this chain are also supported by the EP37-3FLFAO thermal epoxy to fill out any surface imperfections in the radiator and clamps. Both the controller and the supporting components for the spacecraft share similar operating temperatures, and so following testing were deemed appropriate to share a radiator. Evaluation of the controller chain was similar to that of the detector chain (expanded on in the following sections), with hot, warm, and cold cases generated from maximum and idle power consumption cases for the supporting components compared to the same for the controller. The internal heat load on the controller radiator will be much higher than that of the detector radiator, but the operating temperature ranges are much higher and require less precision over time. The supporting components, seen in Figure 3.9, are separated by spacers that connect with the radiator using interfacing spacers.

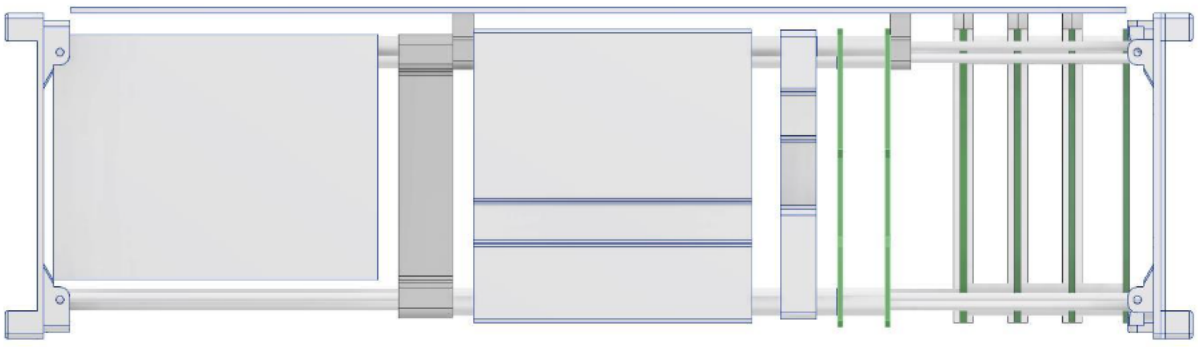

Figure 3.9: Supporting Components (leftmost 2U) with the Controller Chain (rightmost 1U)

In Figure 3.2b a simplified model of Figure 3.10 is shown with all holes removed and any

complicated geometry (round corners, cut-outs and cut corners) simplified using Thermal Desktop and its 2D mesh creation functions. Thermal Desktop's TDMESH function was used to generate a tetrahedral mesh, particularly for the thermal strap geometry. Examples of this are shown in Fig. 3.11 as a comparison between imported Inventor CAD geometry and Thermal Desktop meshes.

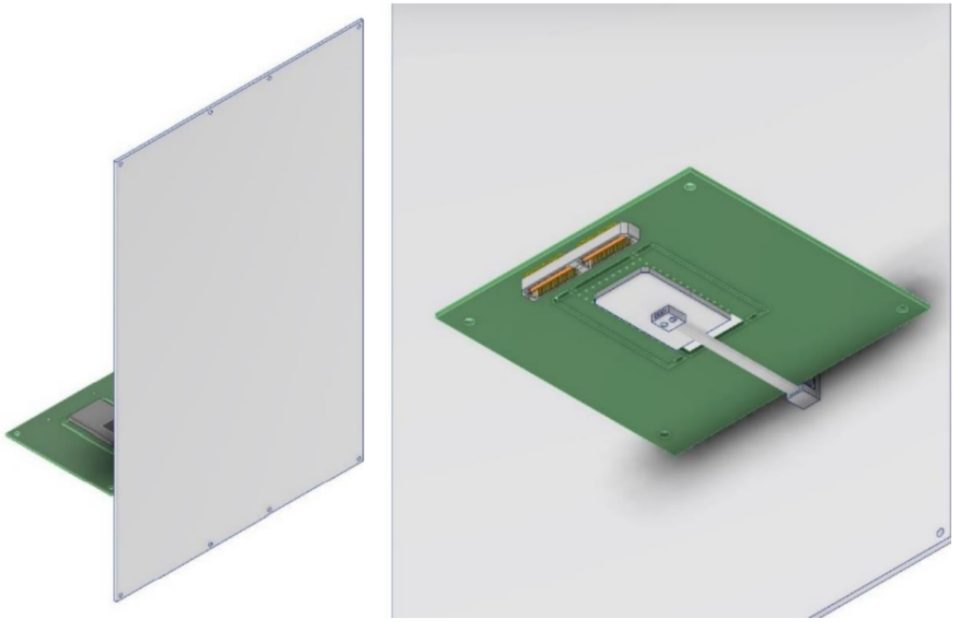

Figure 3.10: CAD render of the detector chain, from the CCD sensor to the radiator

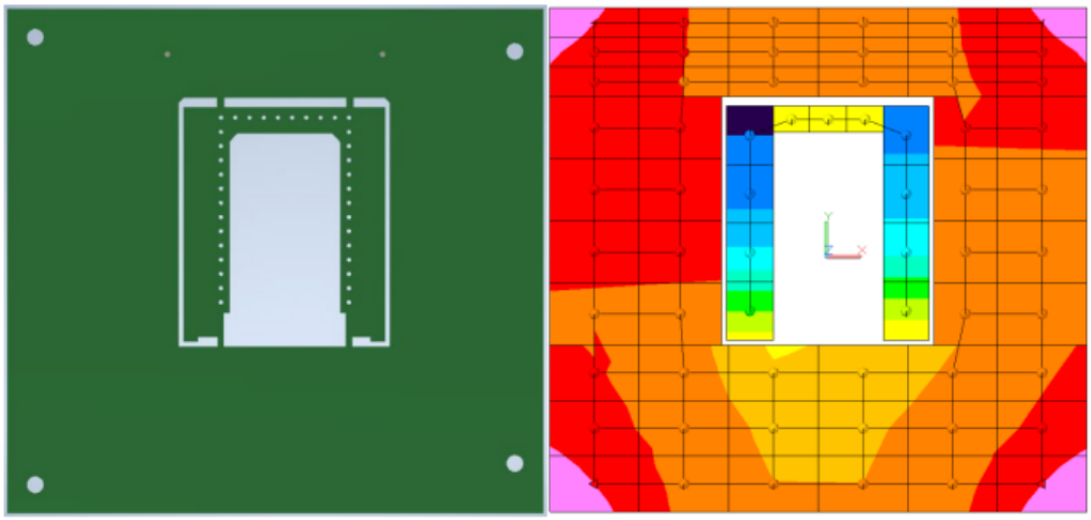

Figure 3.11: Headboard CAD in comparison to the modified Thermal Desktop mesh

Tetrahedral meshes were avoided where more consistent rectangular meshes could be used in order to minimize processing load while running simulations. In some geometries, the node and element count can become excessive, especially for curved geometry and sharp corners. Having such a high element count causes significant slowdown in the SINDA/FLUINT process for transient and steady-state analyses. Figure 3.12 shows the difference between the hand-crafted rectangular mesh of the headboard and the auto-generated tetrahedral mesh of the thermal strap.

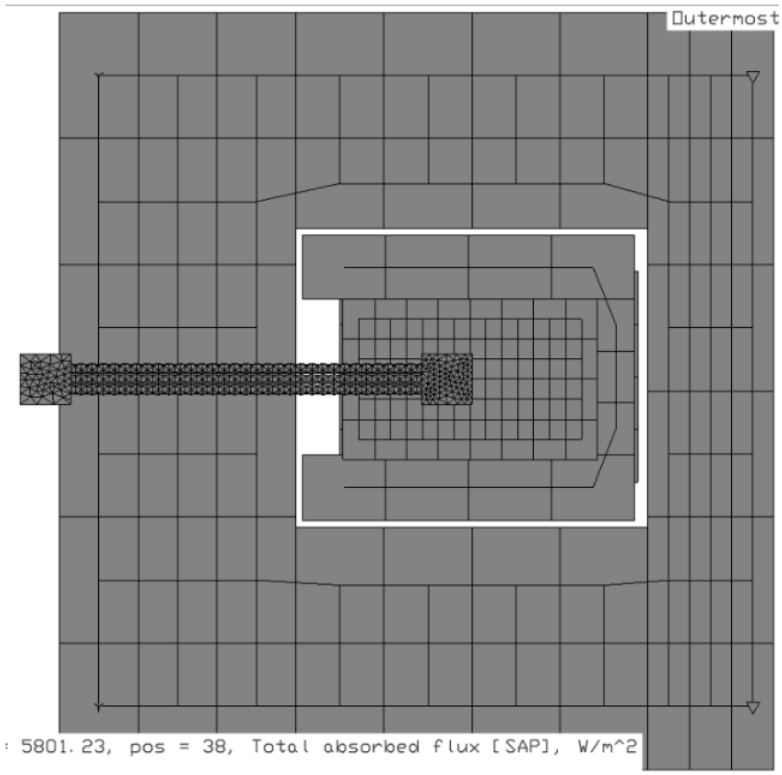

Figure 3.12: Mesh Type Differences in Thermal Strap and Headboard geometry

The simple and open rectangular layout of the nodes and elements in the headboard is contrasted by the dense, cluttered and triangular layout of the thermal strap. This is sometimes necessary for critical components that require more nodes for accurate thermal gradient results, however it should be avoided whenever possible to reduce simulation run time.

Below, the system assumptions and configurations for these simulations are listed:

Table 3.3: Detector Chain Material Characteristics, * = @ $188K$, ** = In the X,Y and Z directions respectively

	Material	Thermal Cond. $[\frac{W}{m \cdot K}]$	Specific Heat $[\frac{J}{kg \cdot K}]$	Density $[\frac{kg}{m^3}]$	Ref. #
Detector	Alumina 94%	18	880	3,690	[1]
Headboard	FR-4 Substrate	0.81, 0.29**	1,150	1,850	[31] [37]
Heatsink	Aluminum 6061	237*	813.4*	2,720	[36] [25] [35]
Thermal Strap	Aluminum 6061	237*	813.4*	2,720	[36] [25] [35]
Thermal Epoxy	EP37-3FLFAO	1.44	1,110	1,110	[21]
Radiator	Aluminum 6061	237*	813.4*	2,720	[36] [25] [35]

Table 3.4: Controller Chain Material Characteristics, * = @ $188K$, ** = In the X,Y and Z directions respectively

	Material	Thermal Cond. $[\frac{W}{m \cdot K}]$	Specific Heat $[\frac{J}{kg \cdot K}]$	Density $[\frac{kg}{m^3}]$	Ref. #
Controller Boards	FR-4 Substrate	0.81, 0.29**	1,150	1,850	[31] [37]
Interface Clamps	Aluminum 6061	237*	813.4*	2,720	[36] [25] [35]
Interface Spacers	Aluminum 6061	237*	813.4*	2,720	[36] [25] [35]
Radiator	Aluminum 6061	237*	813.4*	2,720	[36] [25] [35]
Detector IR Shield	Aluminum 6061	237*	813.4*	2,720	[36] [25] [35]

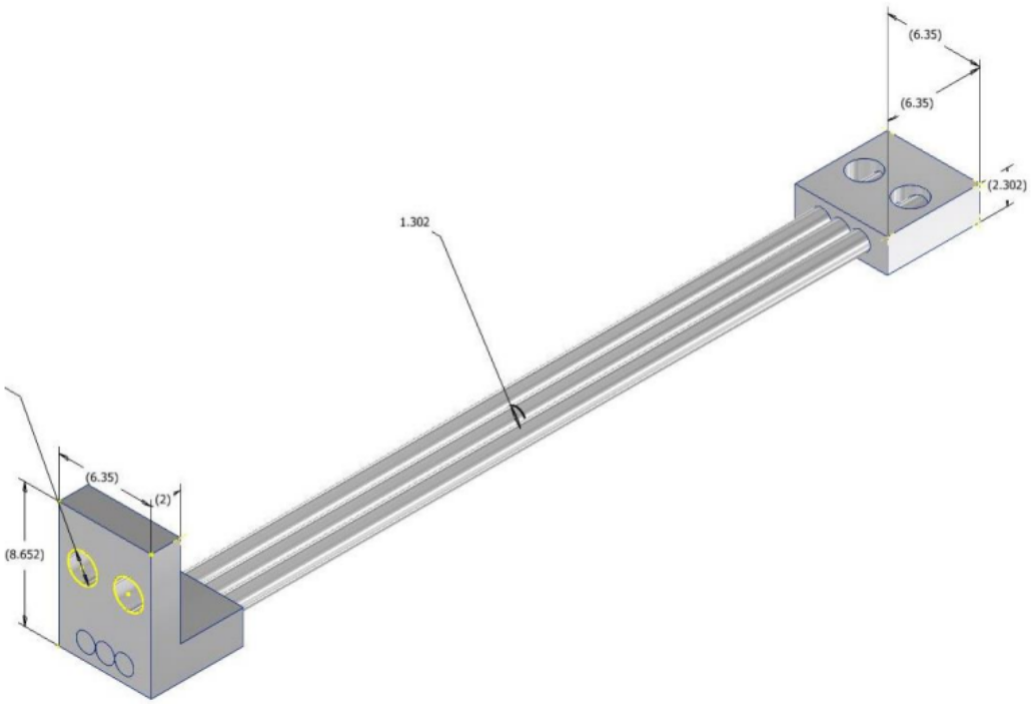

Figure 3.13: Thermal Strap CAD reference (all units in mm)

The thermal strap was designed with a desired dissipation of 0.4W for the operating temperature of -85°C (188.15 K). This dissipation yields a conductance of $G_{TS} = 0.002126\frac{W}{K}$. The necessary dimensions were calculated using the standard equation, $G_{TS} = \frac{\kappa A}{L}\eta_p\eta_s\eta_e$, where the η terms represent the packing efficiency, shape efficiency and end-piece efficiency, respectively. The packing efficiency compares the braided cable, with voids and open space between each individual wire, to that of a solid cylinder, and this can range from 0.5 to 1 for simplicity. The shape efficiency compares the bend of the braided cable to a straight cylinder, and this can range from 0.5 to 1, where 1 is a straight cable and 0.5 is a 180-degree bend. The end piece efficiency qualifies the medium transfer between the clamped braided cable and the end pieces that are used for fastening to a component, and this can vary between 0.75 and 0.99, as no end piece is a pure block of aluminum even though soldered end pieces closely approximate this. Figure 3.13 above shows the CAD model of the detector thermal strap without any bends (i.e. shape factor $\eta_s = 1$). The diameter of the braided cable is exceptionally small, but manufacturable by vendors such as Technology Applications Inc by custom order.

Post-meshing, the model is processed, including the application of heat loads. Two key heat loads are applied for the following analyses: the IR heat load from the warm controller and the internal generation of the detector. A temperature boundary condition is also applied on the nodes that correspond to the chassis rails, and these node temperatures are varied in the three aforementioned cold, warm, and hot cases.

- Controller IR Dissipation: 0.1W ($\epsilon = 0.05$ for polished aluminum shield, controller temperature at 253.15 K, area of shield is A ~$0.008m^2$, $\dot{Q}_{rad} = \epsilon\sigma T^4 A$, constant)

- Detector Heat Dissipation: $0.3W$ (volume distributed, constant), controller-to-detector (FlexLink) cable heat input from controller included here; breakdown: $150mW$ from

Detector at full frame, continuous acquisition and $50mW$ (x3 for safety factor) from the FlexLink controller connection

- Boundary Nodes corresponding to the chassis rails kept at constant temperatures, which vary depending on simulation run (Cold, Warm and Hot cases, covered in more detail below for each case)

Thermal conduction paths must be built by hand in Thermal Desktop. Each interface between surfaces must be specified and given conduction coefficients. These coefficients can be calculated by hand directly input into the system or can be completed by material properties and thickness of the interface. For these analyses, there are 8 individual conduction paths:

1. Detector → Heatsink
2. Heatsink → Thermal Strap End-Piece
3. Thermal Strap End-Piece → Thermal Cables
4. Thermal Cables → End-Piece
5. End-Piece → Radiator
6. Headboard → Detector
7. Lower Headboard → Headboard Inner Conduction Paths
8. Upper Headboard → Headboard Inner Conduction Paths

Alongside heat loads, the environmental loads acting on the system must also be established. For these analyses the environment is simple with just a deep space assumption for external radiation surfaces with a 2.73K sink. As previously covered, propagating orbits will be added in the next stage of simulation resulting in more refining calculations of direct solar, Earth IR and albedo effects.

Chapter 4

Results

4.1 Controller Chain Steady State and Transient Results

The controller chain consisted of the 4-board stack, the -Z chassis, the chassis rails for interfacing, the stack-radiator interface clamps, and the radiator itself, as shown below in Figure 4.1

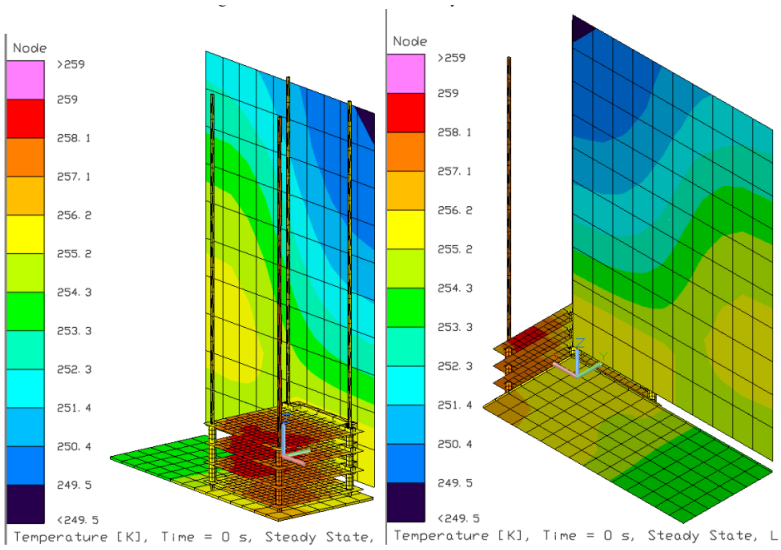

Figure 4.1: Controller Chain Mesh within Thermal Desktop

All of the controller chain simulations were done with orbital effects in consideration as they required the most accurate boundary conditions for qualifying the system. A total of 13

simulation runs were performed with this system, including all three pointing and heating cases (Cold, Warm, and Hot). The goal of these simulations was to ensure that even in the worst heating and pointing case possible for the system, the radiator and board stack were cold-biased in the steady-state and thus heater controllable. The following three figures show the final Hot case results. For this case, the -Z face always faced the Sun and all other axes were able to rotate freely. The following table and figures show the three final simulation runs of the Hot case, this time including a necessary typical parasitic heat load from the supporting components designed to share the radiator with the controller stack. These components are the EPS, ADCS, OBC, payload interface board, and two radios, providing a typical heat dissipation based on power consumption of around $10W$, and a worst case scenario dissipation of $20W$.

Table 4.1: Active Steady State Results for the Controller Chain

Supporting Electronics Input Power (W)	Maximum Controller Temperature (K)	Desired Controller Temperature (min. of Range) (K)	Temperature Delta (K)
0	235.2024	253.15	-17.9476
10	258.9846	253.15	+5.8346
20	270.2653	253.15	+17.1153

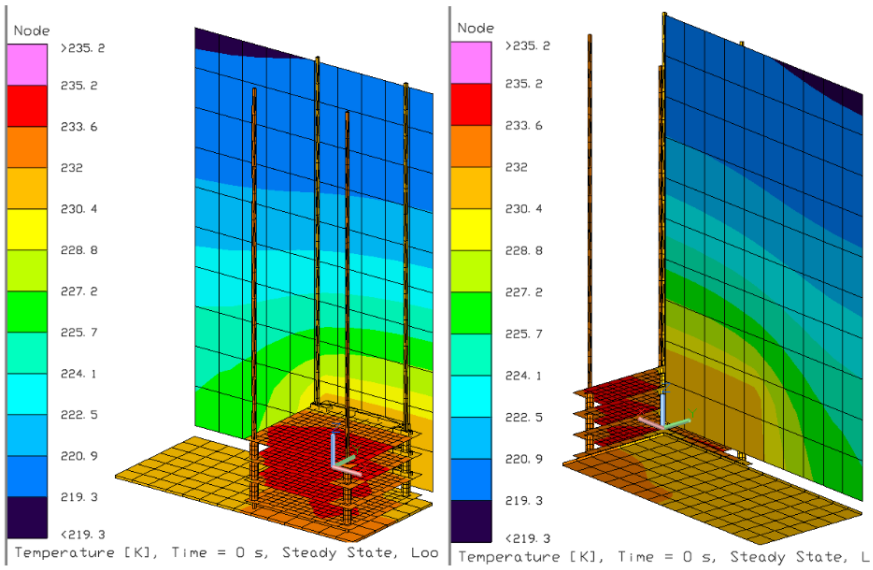

Figure 4.2: ISO View of the Controller Chain Temperature vs. Time, Supporting Heat Input = 0W

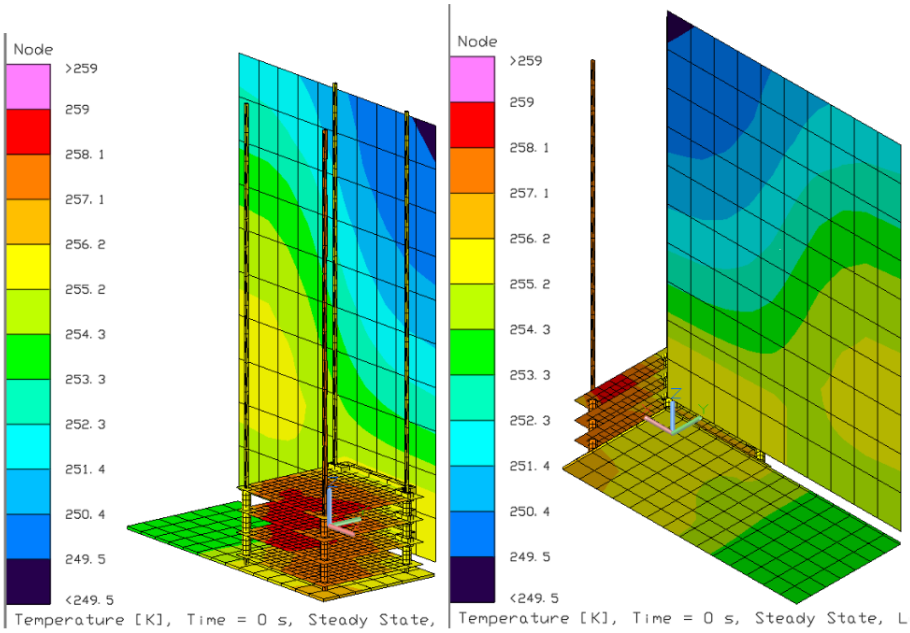

Figure 4.3: ISO View of the Controller Chain Temperature vs. Time, Supporting Heat Input = 10W

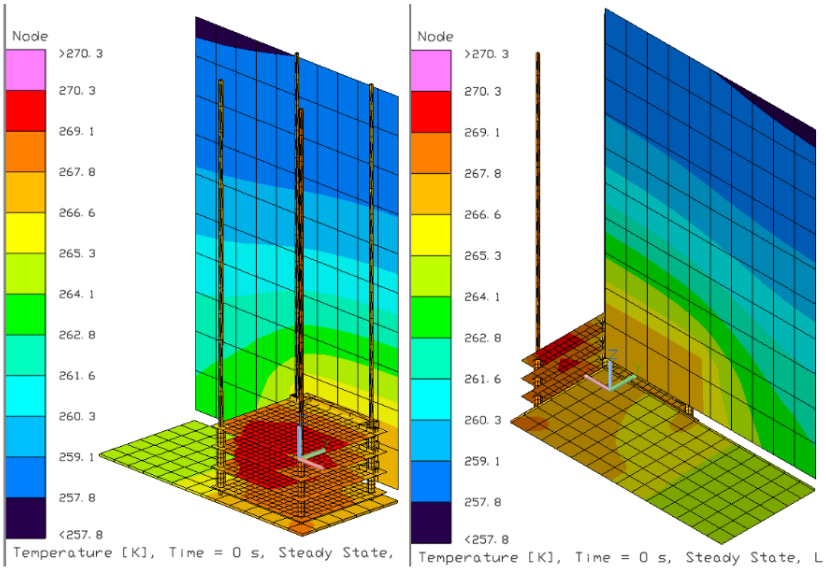

Figure 4.4: ISO View of the Controller Chain Temperature vs. Time, Supporting Heat Input = 20W

These results are promising, as with no parasitic load from the supporting electronics on the radiator we have a cold-biased passive system compared to the minimum desired operational temperature for the controller. These results also mean that the controller temperature can actively be controlled with resistive film heaters. On the other hand, with parasitic loads from the supporting electronics the maximum temperature ends up around 270 K, which is well within the controller operating range of 253.15K to 318.15K, or -20°C to +45°C. This result would allow the system to either not have to input heat with resistive film heaters and save power or warm it further to a more desired temperature within that range. Keep in mind that these results correspond to the Hot case, and that results for the Warm and Cold case showed cooler temperatures. The key to this is that so long the system is colder than our desired temperature range we can use active methods to heat it back into the desired range. The same can not be said for the opposite case, as we can not actively cool our system without the use of a thermoelectric cooler or cryocooler, both solutions that consume too much power to be feasible for a mission such as this.

4.2 Detector Chain Steady State and Transient Results

A total of 9 steady-state simulations were run with Thermal Desktop. The first 3 simulations consisted of the passive behavior of the detector chain, split by case: Cold, Warm and Hot. These results represent the steady-state temperature of the detector chain with specific focus for the center pixel node on the +Z face of the detector. There are no orbital influences acting for these simulations, simply just radiation towards deep space with a temperature of 2.73K. The results are shown in the table below.

Table 4.2: Passive Steady State Results for the Detector Chain

Boundary Rail Nodes Temperature (K)	Steady State Temperature (K)	Initial Radiator Output (W)	Final Radiator Output (W)
253.15 ($-20°C$)	**51.174** ($-221.976°C$)	2.474	0.021
273.15 ($0°C$)	**52.418** ($-220.732°C$)	2.474	0.023
293.15 ($+20°C$)	**53.596** ($-219.554°C$)	2.474	0.0255

The radiator output in Watts is tracked to indicate the importance of the temperature of the radiator for how much it dissipates into a constant background temperature of 2.73K. The passive results show a steady state around 50K, with only a single Kelvin increase as the rail temperatures, corresponding to the controller temperature and ideal conduction through the chassis rails, increase. This indicates that there is already an effective insulating effect between the chassis rails and the detector headboard.

The following 6 simulations focused on the active behavior of the detector chain. There are two simulations per case, one where the internal heater is turned on with a constant output of 0.5W and the other with the heater on at a constant 1W. The goal of these simulations was to ensure the heater can overcome the cooling rate of the radiator without any orbital

effects and starting from the coldest steady-state case results, i.e., the coldest case possible for the system. The results are shown below in Table 4.2 and Table 4.3.

Table 4.3: Active Steady State Results for the Detector Chain, Resistive Heater Input = 0.5W

Boundary Rail Nodes Temperature (K)	Steady State Temperature (K)	Initial Radiator Output (W)	Final Radiator Output (W)
253.15 ($-20°C$)	**149.19** ($-123.96°C$)	2.474	1.534
273.15 ($0°C$)	**149.42** ($-123.73°C$)	2.474	1.543
293.15 ($+20°C$)	**149.658** ($-123.492°C$)	2.474	1.553

Table 4.4: Active Steady State Results for the Detector Chain, Resistive Heater Input = 1W

Boundary Rail Nodes Temperature (K)	Steady State Temperature (K)	Initial Radiator Output (W)	Final Radiator Output (W)
253.15 ($-20°C$)	**204.95** ($-68.2°C$)	2.474	5.463
273.15 ($0°C$)	**205.145** ($-68.005°C$)	2.474	5.483
293.15 ($+20°C$)	**205.339** ($-67.811°C$)	2.474	5.504

These results show that with heater input there is an increased steady-state temperature for the detector, and a similar trend increase for each case as we saw in the passive results. This indicates that the heater can indeed surpass the cooling rate of the radiator in the coldest state possible, proving temperature control with a lack of orbital effects.

Next, transient simulations were run to get a better understanding of the time-dependent behavior of the detector chain. The simulations start at the coldest possible passive case once more and are split into two cases similar to the active cases with the heater at 0.5W and 1W. The length of each simulation is kept to one orbit period, or 5,860 seconds, to minimize the simulation run time. The results are shown below in Figures 4.1 and 4.2.

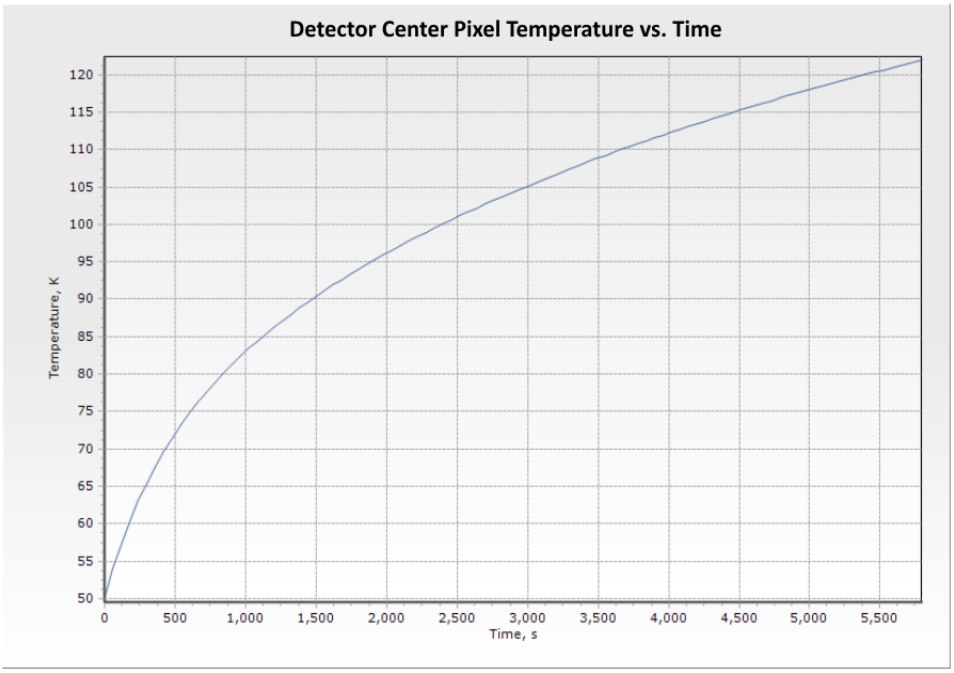

Figure 4.5: Detector Center Pixel Temperature vs. Time, Heater Input = 0.5 W

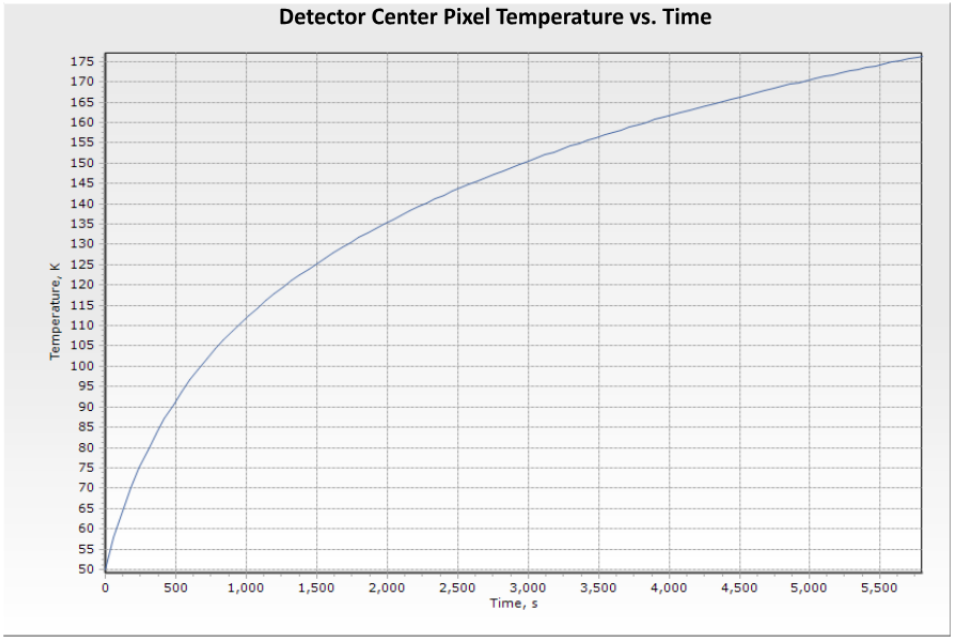

Figure 4.6: Detector Center Pixel Temperature vs. Time, Heater Input = 1 W

These results show as expected the time-dependent temperature of the center pixel of the

+Z face of the detector over one orbit period. From the results it is clear that one orbit is not enough time to reach a steady state and thus we do not see the results as listed in Tables 4.2 and 4.3. Keep in mind that these results still do not consider the orbital environment, which will change the results seen here. In total these simulations took 16 hours to run back-to-back, which also indicates that the simulations can be made more efficient in future iterations.

Finally, for the detector chain we ran extended transient simulations allowing for 4 orbits of simulation time in the hopes of seeing the system transition from transient to steady state behavior. These simulations were run within an orbital environment, so we expect to see oscillatory behavior with the lack of any control scheme implementation. These simulations were run three times, one with no heater input, the second with 0.1W of heater input, and the third run with 0.5W of heater input. The results are shown below in Figure 4.3, Figure 4.4 and Figure 4.5. Keep in mind that these were again run from a starting point of the coldest passive steady state case.

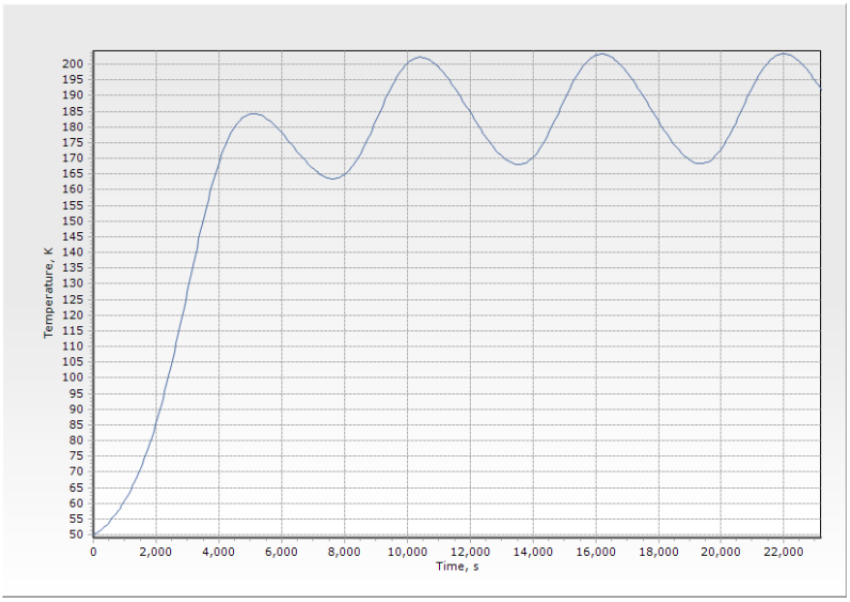

Figure 4.7: Detector Center Pixel Temperature vs. Time, Heater Input = 0W

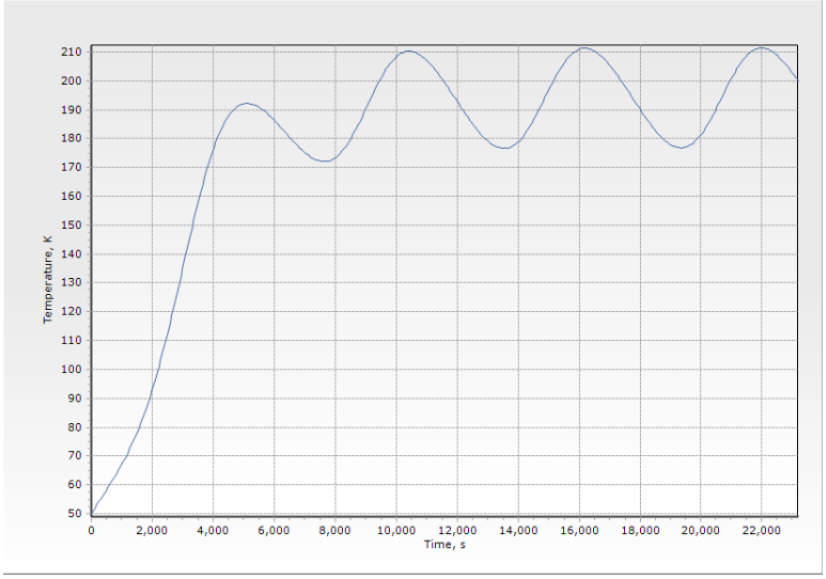

Figure 4.8: Detector Center Pixel Temperature vs. Time, Heater Input = 0.1W

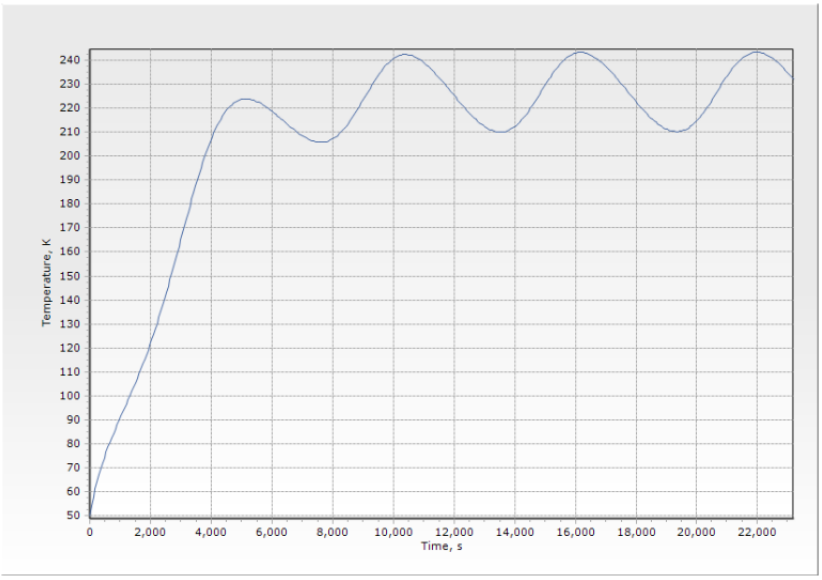

Figure 4.9: Detector Center Pixel Temperature vs. Time, Heater Input = 0.5W

The results show that the detector chain reaches a steady state after 2 orbits, and an oscillation due to entering and exiting the Earth's eclipse is seen as expected. The system oscillates with a change in temperature of roughly $33K$, and the values for each case are

recorded below in Table 4.4.

Table 4.5: Summary of Detector Chain Transient Results

Heater Input (W)	Center Pixel Temperature Range (K)	Mean Temperature (K)
0	168 - 203	185.5
0.1	177 - 211.34	194.17
0.5	210 - 243	226.5

With no heat input and orbital effects accounted for, the mean temperature sits only 2.65 K below the desired temperature of 188.15 K, or -85°C. However, the temperature variance is too far outside of our desired stability of +/-0.25°C. While these results show that a heat input of 0.5W or less is necessary to raise the temperature of the detector, a PID or similar control scheme will be necessary to dampen the amplitude of the oscillations from the periodic passages through eclipse. Further development of such a control scheme within Thermal Desktop for these simulations is considered work for future development.

4.3 Combined Chain Steady State and Transient Results

Finally, the Controller chain and the Detector chain were combined into one mesh within Thermal Desktop to run simulations of the full system. The full combined mesh profile is shown in the figure below.

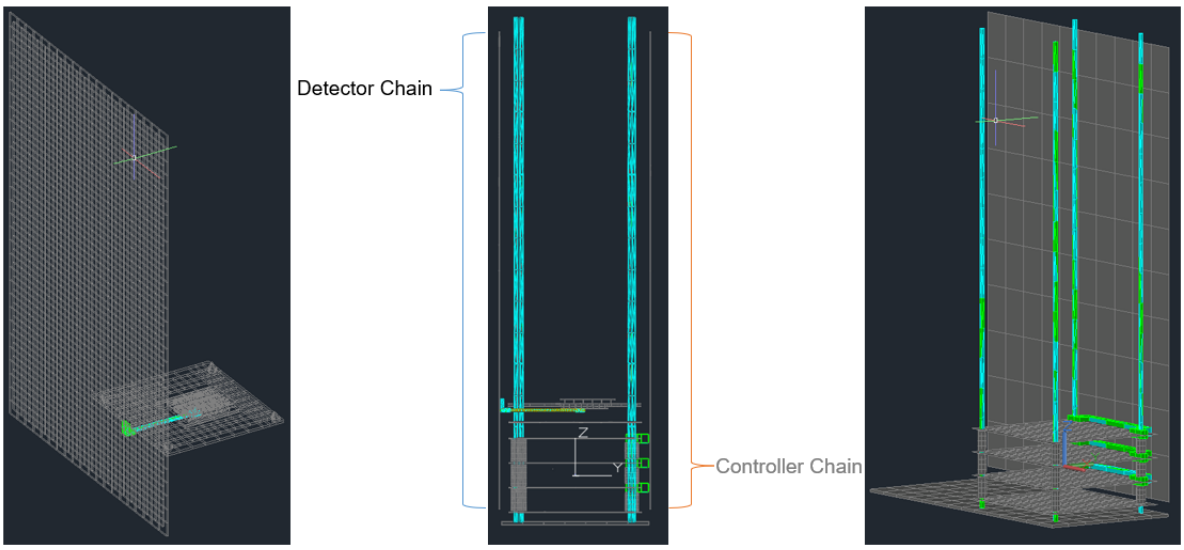

Figure 4.10: The detector, controller and combined meshes shown together in Thermal Desktop

The goal with these simulations is to find the performance of the full system in the worst case scenario for both subsystems, i.e. the hottest possible state for the detector and the hottest pointing case for the controller system. If the controller chain can keep the stack within its range of $253.15K$ to $318.15K$, or $-20°C$ to $+45°C$, and show that the detector chain can remain colder than the desired temperature range of $188.15 \pm 0.25K$, or $-85 \pm 0.25°C$, then the system is controllable. For this reason, the pointing assumptions have the -Z axis of the combined system aligned with the solar vector while the other axes are given a rotation rate of $1\frac{rad}{sec}$.

The following figures show the results of the first steady state simulation of the combined chain. For this run, the following was true:

- Detector Heatsink Heater Power: $0W$
- Support Components Heat Load: $0W$
- Controller Board Internal Generation: $12.5925W$

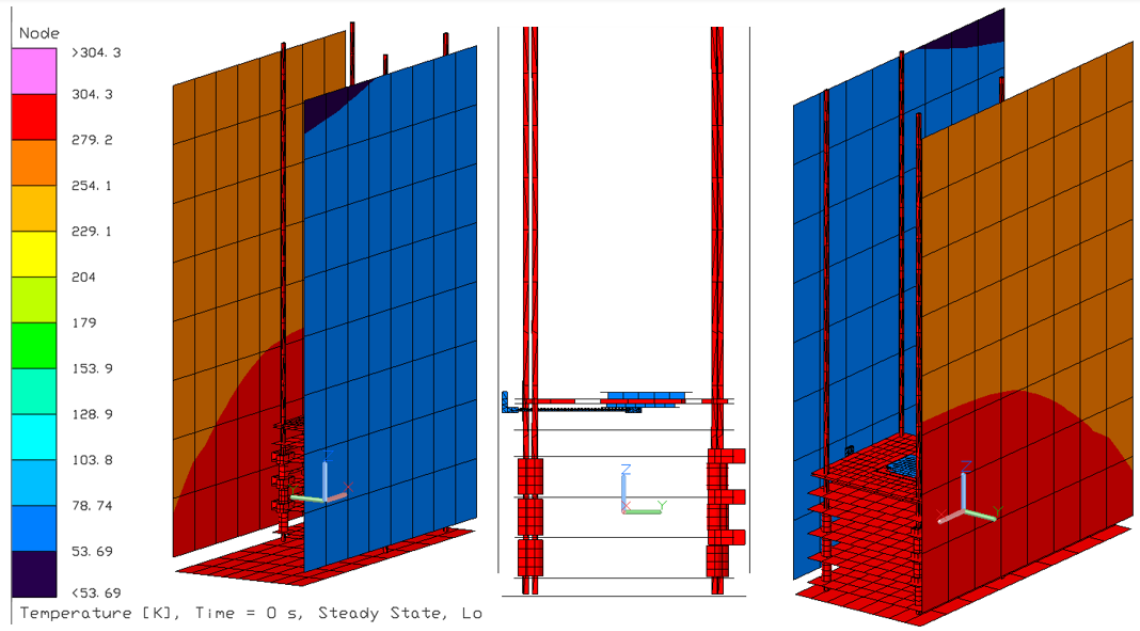

Figure 4.11: The detector, controller and combined meshes with the steady state heat gradient overlaid

Table 4.6: Summary of Combined Chain Results for Steady State Simulation A

Controller Component	Controller Board Temperature Range (K)	Detector Center Pixel Temperature (K)
CCD Drive Board	295.167 - 300.356	
Vertical Drive Board	295.321 - 300.155	
Digital Drive Board	295.326 - 300.077	
Power Board	291.167 - 299.333	
		62.4185

The following figures show the results of the second steady state simulation of the combined chain. For this run, the following was true:

- Detector Heatsink Heater Power: $0W$
- Support Components Heat Load: $10W$
- Controller Board Internal Generation: $12.5925W$

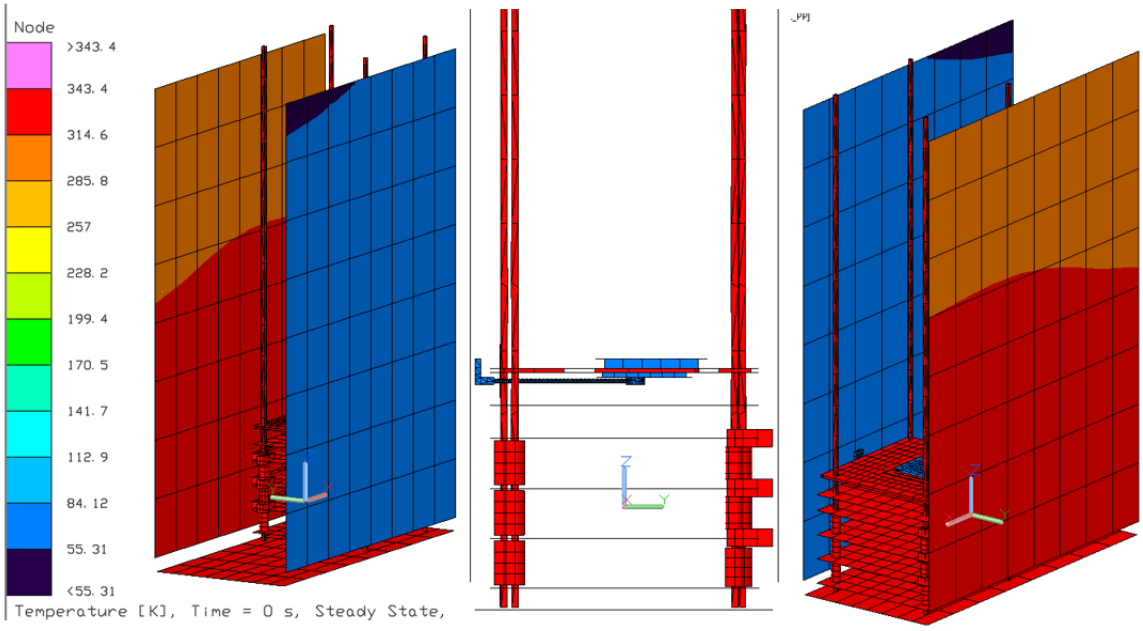

Figure 4.12: The detector, controller and combined meshes with the steady state heat gradient overlaid

Table 4.7: Summary of Combined Chain Results for Steady State Simulation B

Controller Component	Controller Board Temperature Range (K)	Detector Center Pixel Temperature (K)
CCD Drive Board	335.2094 - 339.7205	
Vertical Drive Board	335.2884 - 339.446	
Digital Drive Board	335.2896 – 339.3616	
Power Board	335.2807 – 338.5905	
		63.8364

Following the results of these two tests, it can be seen that the detector can indeed be passively cooled and sit at a temperature lower than the desired operational temperature, indicating that it can be controlled with a resistive heater. In previous results, it was shown that the detector requires a very small constant heat input, less than $0.1W$, to reach a median temperature close to the desired temperature of $188.15K$. This all points to a low power solution for temperature control with a scheme such as PID. The results also show

that the controller must share a parasitic load from the supporting CubeSat components of less than $10W$, and indeed closer to $0W$, in order to sit within the desired temperature range of 253.15 - 318.15K.

Chapter 5

Conclusions

5.1 Conclusion

For this program we have focused on the thermal challenges of developing a 6U CubeSat platform for an EMCCD payload developed by Nüvü Camēras. These challenges came primarily from the platform itself, as CubeSats have significantly less volume, surface area, mass and power available to them as compared to conventional spacecraft. The system was split into two components, the detector chain and the controller chain, which are isolated from each other and correspond to very different requirements. In simulating each chain within Thermal Desktop, it was found that a cold-biased passive system with resistive film heaters for active control are sufficient to reach the desired temperature range. Further research into dampening the orbital temperature variation at steady state to within +/- 0.25°C is ongoing by Nüvü Camēras with various control schemes, including PID control. Once a full thermal system is qualified within Thermal Desktop, a full example 6U CubeSat will be developed, including all supporting electronics for a sun-synchronous orbit mission.

5.2 Risk Management

During the development phase of this project multiple constraints were implemented. Chief among these was the pointing constraint implemented to control exposure of the 6U radiator

panels to direct solar, albedo, and Earth IR effects. This did not take into account any form of observation tasking, which would require deviation from those strict pointing requirements. Any change in pointing while exposed to sunlight could present a significant increase in thermal load on the radiators and raise the steady state temperature of the system. The same effect occurs with increased albedo and Earth IR exposure, albeit to a lesser magnitude. The extent of the increase requires additional simulation earmarked for future work. One potential solution discussed during development was to restrict observations to periods of eclipse. This removes the potential for exposure to direct sunlight and albedo effects, but reduces time on target for observations and still leaves Earth IR exposure as an issue. Time in eclipse can vary depending on orbit geometry, and spacecraft attitude rate-of-change can alter how much time you get to observe after you enter and before you leave eclipse. Calculating the magnitude of these effects on operations and the thermal load of the system is necessary to determine how desirable this solution is, and this would be an objective for future work.

A second major risk for this system is the structural efficacy of the inner headboard design. The thermal isolation of the detector from the rest of the headboard, and thus the heat leakage from the rest of the spacecraft, provided by the cutout leaves the detector with little structure to connect to. The operational environment in orbit will not have high vibrations or structural loads, but during ground handling and launch this could present an issue. The inner headboard is only supported by four small bridges of FR4, providing exceptional thermal isolation but only minimal structural support. A solution here would be to compromise between thermal isolation and structural stability by either increasing the number of bridges or increasing the width of the current bridges. This would require minimal modeling time and provide potentially significant structural improvement, however the extent of this is in need of further simulation. The detector itself is attached to the inner

headboard via 30 Constantan wires that provide an electrical and thermal connection along with thermal epoxy. The wires are not designed to be a structural support, but the epoxy provides a thermal and highly flexible structural connection. Vibrational and structural load simulations need to be performed to prove the efficacy of these systems, their risks, and their solutions.

5.3 Future Work

5.3.1 Environmental Testing

Upon the completion of the development and simulation phases of the project, a prototype of the payload will be built along with the system and supporting CubeSat. This prototype will undergo environmental tests commensurate with the TRL goal, namely TRL 5 and TRL 6. This testing will take place in two phases, with the first achieving TRL 5 and the second achieving TRL 6. The fulfillment of TRL 5 requires that component level testing shows documented agreement with analytical and simulation predictions, and thanks to the features of Autodesk Inventor and Thermal Desktop, simulations provide predictions for thermal, radiation, and vibration performance. Similarly, the fulfillment of TRL 6 requires a high fidelity prototype and system level testing that shows documented agreement with analytical and simulation predictions.

For both phases, testing will be split into three major components: Thermal Cycling and Thermal Vacuum, Single-Axis and Random Vibration, and Radiation testing. Thermal Cycling and Thermal Vacuum, or TVAC, require a chamber capable of large temperature swings and holding as close to a perfect vacuum as possible while accommodating the prototype. A TVAC chamber capable of meeting these requirements, an example of which are shown in

(a) and (b) of the figure below, is located on the campus of Virginia Tech.

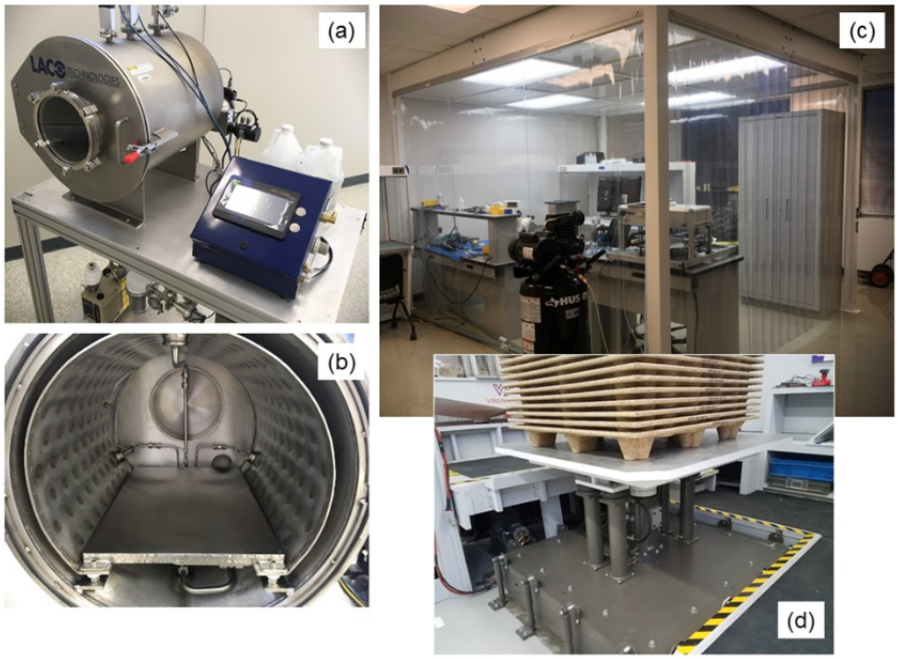

Figure 5.1: (a)+(b) show the Virginia Tech TVAC chamber, sized for 6U CubeSats or smaller, (c) shows the ISO 7 clean room facility from 2018 at Virginia Tech, (d) shows the VT Pallet Lab Lansmont Model 10000 Vibration Tester

The TVAC testing will only take place in the first phase as an approach towards TRL 5 with component level testing. The Nuvu controller and CCD201-20 detector will be tested separately in the chamber with their corresponding thermal chains to the protoflight level. This level is illustrated by the figure below as $\pm 10°C$ of the allowable operational temperature range. The chamber will be kept at a pressure less than $10^{-5} torr$, and the payload chassis will be placed on a temperature controlled platen. A cold finger will be used to achieve the cold temperatures necessary in place of the space environment for testing of the detector. The number of cycles, plateau duration and dwell times, and maximum transition rates will all conform to NASA GEVS [16].

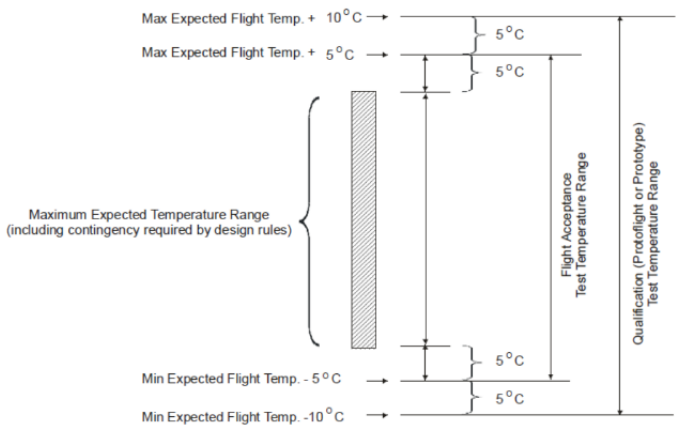

Figure 5.2: Visualisation of the acceptable flight temperature range and the protoflight temperature range for testing

As a part of mandatory testing for components going to space, the controller stack and detector payloads will be tested on a Lansmont Model 10000 vibration table. Each component will undergo a random vibration test along three orthogonal axes for one minute each. Alongside random vibration tests, each component will also undergo sweeping sine wave vibrations in each of the three axes with the requirement that one axis is parallel to the anticipated axis of thrust of the chosen launch vehicle. These tests will follow the Component Minimum Workmanship test levels as seen in NASA GEVS, shown in the figure below [16].

Frequency (Hz)	ASD Level (g^2/Hz)
20	0.01
20-80	+3 dB/oct
80-500	0.04
500-2000	-3 dB/oct
2000	0.01
Overall	6.8 g_{rms}

The plateau acceleration spectral density level (ASD) may be reduced for components weighing between 45.4 and 182 kg, or 100 and 400 pounds according to the component weight (W) up to a maximum of 6 dB as follows:

	Weight in kg	Weight in lb
dB reduction	= 10 log(W/45.4)	10 log(W/100)
$ASD_{(plateau)}$ level	= 0.04•(45.4/W)	0.04•(100/W)

The sloped portions of the spectrum shall be maintained at plus and minus 3 dB/oct. Therefore, the lower and upper break points, or frequencies at the ends of the plateau become:

F_L = 80 (45.4/W) [kg] = 80 (100/W) [lb] F_L = frequency break point low end of plateau

F_H = 500 (W/45.4) [kg] = 500 (W/100) [lb] F_H = frequency break point high end of plateau

The test spectrum shall not go below 0.01 g^2/Hz. For components whose weight is greater than 182-kg or 400 pounds, the workmanship test spectrum is 0.01 g^2/Hz from 20 to 2000 Hz with an overall level of 4.4 g_{rms}.

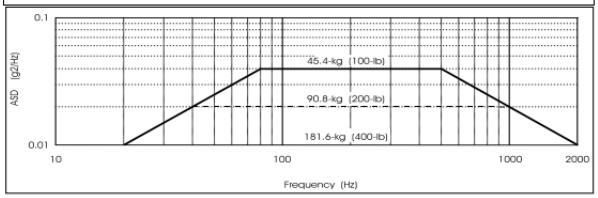

Figure 5.3: Component Minimum Workmanship Random Vibration Test Levels for a payload of 45.4 kg (100 lbs) or less

Radiation testing for each component will consist of Total Ionizing Dose (TID), Neutron Irradiation Displacement Damage Dosage (N/DDD), and Single Event Effects (SEE) testing. TID testing can occur with VPT Rad in Blacksburg, VA with a Cobalt-60 source and the following setup:

- NIST certified traceable alanine dosimetry system
- Dose mapping; uncertainty to within 3% (low and high dose)
- Dose rates from:
  - Low: 0.01 – 15 rad (Si)/s

    - MIL-STD-883/750 Test Method 1019 Condition C and D compliant
    - ELDRS analysis
    - TM-1019 Compliant Pb/Al Containers
  - High: Up to 150 rad (Si)/s
    - MIL-STD-750 & 883 Test Method 1019 A, C and D compliant
    - TM-1019 compliant Pb/Al boxes

N/DDD and SEE testing will occur with the following setup:

- Neutron irradiation testing for DDD
  - MIL-STD-883/750 Test Method 1017
  - Flux range of 1.0E+08 – 1.0E+11 n/cm2-sec (1 MeV equivalent Si)
  - 8" x 8" uniform beam
- Support for heavy ion Single Event Effects
  - Test planning and implementation per ESCC25100 or JESD57
  - MIL-STD 750 Test Method 1080
  - Heavy ion cross sections for components/system

The environmental testing described above would qualify the system for the both the controller stack and the detector to TRL 5, but not TRL 6. In order to achieve TRL 6, the two chains must be combined and tested together using a similar suite of vibration, TVAC, and radiation trials.

5.3.2 Control

The goal of this project was to design a temperature management system for a near-cryogenic camera developed for a CubeSat form factor. Every component of the payload, from the camera detector to the hundredth resistor on the camera controller, has a temperature range in which it can operate at with known performance characteristics. This control system is designed to get the temperature of each component of the payload to its desired operating or performance temperature range and keep it there to within a desired tolerance. To do this, control theory can be applied. Control theory itself is well established and documented, but for this project two methods were considered: 2-Step and PID.

2-Step control is also known as bang bang, hysteresis, or on-off control. It is a discontinuous feedback control method that switches between two states, like a light switch, based on a set threshold or magnitude. A common example of this kind of system is that of a thermostat. A lower and upper temperature threshold is set, and the temperature of the room is monitored by a sensor. Once the temperature reaches or drops below the lower temperature threshold, the thermostat sends a signal to start heating the room. Once the temperature reaches the upper threshold, the thermostat sends a signal to stop heating or to start cooling the room. The control system is a cooling fan and heating system, which operates either fully on or off, depending on the detected temperature and set thresholds. This control scheme would work similarly for a cooled camera detector; a temperature sensor placed within a heat sink attached to the detector would provide the tracking, and temperature thresholds set $0.25°C$ above and below $-85°C$ provide the on-off boundaries. In theory, this would provide the desired $-85 \pm 0.25°C$ performance range. However, this method causes sharp, high frequency oscillations between the set thresholds, as seen in Figure 1.5 below, that are harmful to the EM gain performance of the detector, which thrives under stable temperature conditions.

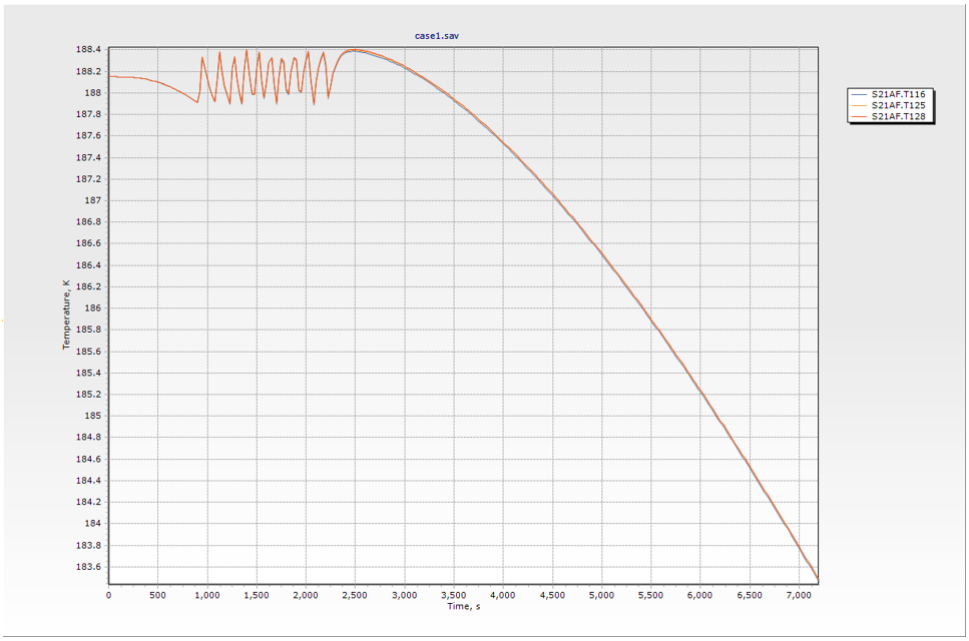

Figure 5.4: 0.5W Heater test with starting temperature of $-85°C$, or $188.15K$

A smooth and stable temperature behavior can be achieved by PID, or Proportional Integral Derivative, control. This control method relies on the variation of an error term, $e(t)$, defined by the difference between a set point, $SP(t)$ and a measured value, $MV(t)$, as seen below [30].

$$e(t) = SP(t) - MV(t) \tag{5.1}$$

In this case, the set point would be a temperature of $188.15K$, or $-85°C$, and the measured value would be the input from the heat sink thermocouple. This error term would be manipulated into three separate driving equations, $u_P(t)$, $u_I(t)$, and $u_D(t)$, which are then summed up into an input signal for controlling the resistive heater in the heat sink. Mathematically, these equations take the forms shown below [30],

$$u_P(t) = K_P e(t) \tag{5.2}$$

$$u_I(t) = K_I \int_0^t e(\tau) d\tau \tag{5.3}$$

$$u_D(t) = K_D \frac{d}{dt} e(t) \tag{5.4}$$

Where the K_P, K_I, and K_D terms are dimensionless weight coefficients that allow the user to define how much of each to affect the overall driving equation,

$$u(t) = u_P(t) + u_I(t) + u_D(t) \tag{5.5}$$

With PID control, a heater can be fed different current values, and therefore different power output values, based on the measured temperature difference from the set point. In this way, the heater can be on at a spectrum of values as opposed to just on and off at full power. This provides smooth temperature behavior, avoiding any sharp spikes and unpredictable detector performance. The figure below shows a visual representation of the PID control loop [30].

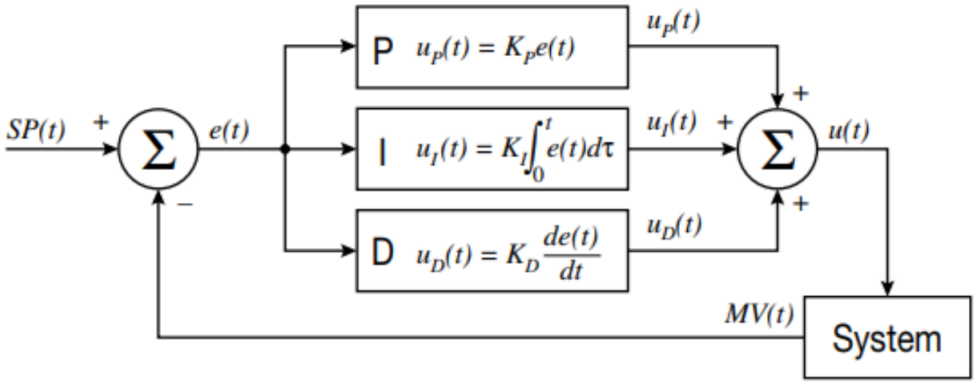

Figure 5.5: PID Block Diagram

Bibliography

[1] Accuratus. Aluminum oxide, al2o3 ceramic properties, 2016. URL https://accuratus.com/alumox.html.

[2] G.B. Arfken, D.C. Kelly, D.F. Griffing, and J. Priest. *23.1 - Conduction*. International Edition University Physics, Elsevier, 1st edition, 1984.

[3] M. Bahrami. Steady conduction heat transfer, 2009. URL https://www.sfu.ca/~mbahrami/ENSC%20388/Notes/Staedy%20Conduction%20Heat%20Transfer.pdf.

[4] W.S. Boyle and G.E. Smith. Charged coupled semiconductor devices. *Bell System Technical Journal*, 49(4):587–593, 1970. doi: https://doi.org/10.1002/j.1538-7305.1970.tb01790.

[5] S. Caldwell. 7.0 - thermal control, 2021. URL https://www.nasa.gov/smallsat-institute/sst-soa/thermal-control.

[6] O. Daigle. Emccd tutorial: Nuvu cameras, 2017. URL https://www.nuvucameras.com/emccd-tutorial/.

[7] O. Daigle and et. al. Nancy grace roman space telescope coronagraph emccd flight camera electronics development. *Space Telescopes and Instrumentation 2022: Optical, Infrared, and Millimeter Wave*, 2022. doi: https://doi.org/10.1117/12.2626242.

[8] O. Daigle and L.K. Harding. Nuvu cameras - virginia tech | statement of work. 2021.

[9] A. de Rooij. Corrosion in space, 2010. URL http://esmat.esa.int/Publications/Published_papers/Corrosion_in_Space.pdf.

[10] C. Engel. Heat transfer chapter 3: Steady heat conduction, 2010. URL http://www.cecs.wright.edu/~sthomas/htchapter03.pdf.

[11] ESA. Planck and the cosmic microwave background, 2013. URL https://www.esa.int/Science_Exploration/Space_Science/Planck/Planck_and_the_cosmic_microwave_background#:~:text=Planck's%20predecessors%20(NASA's%20COBE%20and,almost%20everywhere%20on%20the%20sky.

[12] Banks. B.A. et. al. Simulation of the low earth orbital atomic oxygen interaction with materials by means of an oxygen ion beam, 1989. URL https://ntrs.nasa.gov/api/citations/19890011733/downloads/19890011733.pdf.

[13] J. Foley. Cubesat standard, 2016. URL https://www.cubesat.org/about.

[14] S.M. Gilbert, L.M. & Scala. Free molecular heat transfer in the ionosphere. *NASA NTRS*, 18:283–303, 1965. doi: https://doi.org/10.1016/b978-1-4831-9754-8.50009-4.

[15] G.A. Greene. Free molecular heat transfer near a wall. *Encyclopedia of Physical Science and Technology*, 3:279–292, 2003.

[16] NASA GSFC. General environmental verification standard for gsfc flight programs, 2021. URL https://standards.nasa.gov/sites/default/files/standards/GSFC/B/0/gsfc-std-7000b_signature_cycle_04_28_2021_fixed_links.pdf.

[17] R. Jimenez. Effects of natural environment charged particle heating on the design and performance of spacecraft cryogenic components. *AIAA Thermophysics Conference*, 24, 1989. doi: https://doi.org/10.2514/6.1989-1760.

[18] A. Johnstone. Cubesat design specification revision 14.1, 2022. URL https://static1.squarespace.com/static/5418c831e4b0fa4ecac1bacd/t/62193b7fc9e72e0053f00910/1645820809779/CDS+REV14_1+2022-02-09.pdf.

[19] NASA LaRC. What is albedo?, 2020. URL https://mynasadata.larc.nasa.gov/mini-lessonactivity/what-albedo.

[20] E.T. Malroy. Free molecular heat transfer programs for setup and dynamic updating of conductors in thermal desktop, 2007. URL https://ntrs.nasa.gov/api/citations/20070030243/downloads/20070030243.pdf.

[21] MasterBond. Ep37-3flfao technical data sheet, 2020. URL https://www.masterbond.com/tds/ep37-3flfao.

[22] C. McFee. Noise sources in a ccd, 2002. URL https://www.mssl.ucl.ac.uk/www_detector/ccdgroup/optheory/darkcurrent.html.

[23] NASA. Ssri knowledge base thermal analysis, 2023. URL https://s3vi.ndc.nasa.gov/ssri-kb/topics/15/?types=SOFTWARE#resources.

[24] C.R. Nave. Stefan-boltzmann law, 1998. URL http://hyperphysics.phy-astr.gsu.edu/hbase/thermo/stefan.html.

[25] NIST. Aluminum 6061-t6 (uns aa96061), 2018. URL https://www.nist.gov/mml/acmd/aluminum-6061-t6-uns-aa96061.

[26] NWS. The earth-atmosphere energy balance, 2019. URL https://www.noaa.gov/jetstream/atmosphere/energy.

[27] Patrick H. Oosthuizen and David Naylor. *An Introduction to Convective Heat Transfer Analysis*. WCB/McGraw-Hill, International, 1999.

[28] Ioan Pop and Derek B. Ingham. *Convective Heat Transfer*. Elsevier Ltd., Amsterdam, Netherlands, 2001. doi: https://doi.org/10.1016/B978-0-08-043878-8.X5000-7.

[29] A.K. Rebrov. Free molecular heat transfer near a wall. *AIAA*, 2(1):215–216, 1964. doi: https://doi.org/10.2514/3.2279.

[30] R. Rogers. Building a benchtop pid controller, 2013. URL https://download.tek.com/document/BenchtopPIDController_WhPaper.pdf.

[31] F. Sarvar, N.J. Poole, and P.A. Witting. Pcb glass-fibre laminates: Thermal conductivity measurements and their effect on simulation. *Journal of Electronic Materials*, 19: 1345–1350, 1990. doi: https://doi.org/10.1007/BF02662823.

[32] Physical Society. Societies and academies. *Nature*, 66:118–120, 1902. doi: https://doi.org/10.1038/066118b0.

[33] ESA TEC-SHS. Esa trl handbook. 2008.

[34] AZ Technologies. Az93 white thermal control, inorganic paint/coating, 2021. URL https://www.aztechnology.com/product/1/az-93.

[35] Engineering Toolbox. Metals and alloys - densities, 2014. URL https://www.engineeringtoolbox.com/metal-alloys-densities-d_50.html.

[36] Engineering Toolbox. Metals, metallic elements and alloys - thermal conductivities, 2014. URL https://www.engineeringtoolbox.com/thermal-conductivity-metals-d_858.html.

[37] T. Uygunoglu, I. Gunes, and W. Brostow. Physical and mechanical properties of polymer composites with high content of wastes including boron. *Materials Research*, 18: 1188–1196, 2015. doi: https://doi.org/10.1590/1516-1439.009815.

Appendices

Appendix A

Appendix

A.1 Additional Information

A.1.1 Objectives and TRL Definition

The objective of this project was to raise the Technology Readiness Level, or TRL, of a space-centric redesign of the Nüvü Camēras' EMCCD up to TRL-5. To give this ranking some context, the Technology Readiness Level is defined as a measurement of the maturity of a technology, from a basic research concept on paper to a flown piece of equipment [33]. This measurement system also allows the comparison of technology maturity for system design decisions. This most often takes the form of higher TRL components being selected for spacecraft than lower TRL components due to the reduced risk to the mission. The following figure shows the definitions of TRL-1 through TRL-6, according to the ESA TRL Handbook [33].

Readiness Level	Definition	Explanation
TRL 1	Basic principles observed and reported	Lowest level of technology readiness. Scientific research begins to be translated into applied research and development. (See Paragraph 4.2)
TRL 2	Technology concept and/or application formulated	Once basic principles are observed, practical applications can be invented and R&D started. Applications are speculative and may be unproven. (See Paragraph 4.3).
TRL 3	Analytical and experimental critical function and/or characteristic proof-of-concept	Active research and development is initiated, including analytical / laboratory studies to validate predictions regarding the technology. (See Paragraph 4.4)
TRL 4	Component and/or breadboard validation in laboratory environment	Basic technological components are integrated to establish that they will work together. (See Paragraph 4.5)
TRL 5	Component and/or breadboard validation in relevant environment	The basic technological components are integrated with reasonably realistic supporting elements so it can be tested in a simulated environment. (See Paragraph 4.6)
TRL 6	System/subsystem model or prototype demonstration in a relevant environment (ground or space)	A representative model or prototype system is tested in a relevant environment. (See Paragraph 4.7)
TRL 7	System prototype demonstration in a space environment	A prototype system that is near, or at, the planned operational system. (See Paragraph 4.8)
TRL 8	Actual system completed and "flight qualified" through test and demonstration (ground or space)	In an actual system, the technology has been proven to work in its final form and under expected conditions. (See Paragraph 4.9)
TRL 9	Actual system "flight proven" through successful mission operations	The system incorporating the new technology in its final form has been used under actual mission conditions. (See Paragraph 4.2.10)

Figure A.1: TRL Handbook basic definitions of each level [33]

As mentioned earlier, the objective of this project was to raise the Nüvü Camēras' EMCCD to TRL 5, or to perform environmental tests, i.e. thermal vacuum, vibration, and radiation, for conditions that match LEO on the EMCCD detector and controller components, with a fully functional temperature management system. The environmental tests and TRL advancement plan will be discussed further in the Future Works portion of the conclusion of this paper.

To achieve these tests and the TRL advancement, a system had to be designed to regulate both the electronics and the EMCCD detector. This took the form of 3D modeling work, MATLAB program development for initial thermal assessment, and in-depth thermal simulation work with dedicated software, which will all be discussed in the following section.